Title
Electrical and Thermoelectrical Transport Properties of Graphene

Author
Wang, Deqi

Publication Date
2011

Peer reviewed|Thesis/dissertation

UNIVERSITY OF CALIFORNIA
RIVERSIDE

Electrical and Thermoelectrical Transport Properties of Graphene

A Dissertation submitted in partial satisfaction
of the requirements for the degree of

Doctor of Philosophy

in

Physics

by

Deqi Wang

August 2011

Dissertation Committee:

Dr. Jing Shi, Chairperson
Dr. Ward Beyermann
Dr. Jeanie Lau

The Dissertation of Deqi Wang is approved:

_____

_____

_____

Committee Chairperson

University of California, Riverside

Acknowledgements

Now it is time to write the acknowledgements! Six-year is not a short time in life. I feel very lucky to study my Ph. D. degree in University of California, Riverside. It is definitely a very meaningful time to for me. What I have got here would be tremendous wealth for me to use in the rest of my life.

First, I would like to thank my Ph. D. advisor, Dr. Jing Shi. Dr. Shi is a great scientist and very supportive to his students. I am very proud to be his student. What I have learned from him are not only the physics, but more importantly, the skills to deal with the real world. Under his guidance, I have developed myself to be an independent physics researcher and a confident fighter who is ready to meet the challenge in the future life. Thank you very much, Dr. Shi.

I would like to thank my committee member, Dr. Ward Beyermann and Dr. Jeanie Lau and my collaborator Dr. Yadong Yin.

I would like to thank my lab mates, Peng Wei, Xinfei Liu, Tao Lin, Ray Sachs, Zhiyong Wang, and Mohamed Hamad and my collaborator Le He. Without their help and useful discussion, this thesis would not be possible.

Also, I would like to thank my friends Yachong Wang, Peng Wei, Hsiang-Ku Lin, Ling Yang, Gang Liu, Yang Meng, Yan Li, James Wu, Christy Yeh, Yihuei Jiang, Hsin-Ying Chiu, Dong Gui, Wenzong Bao, Xiaoxiao He, Wei Han, Tao Lin, Xinfei Liu, Xin He, Fan Zhang, Zhiyong Wang, Lingchao Zhu, Weihua Zhou, Yong Pu, Tongda Xu, Dong Yan, Dexter Humphrey, Di Wu, Ruobo Zhou, Da Pu, Heng Yang, Huwei Zhang. Thank you so much for your support. I enjoyed every moment staying with your guys.

Finally, I would like to express my great gratitude to my parents and sister for their love and support. 爸爸，妈妈，姐姐，谢谢你们，我爱你们！

ABSTRACT OF THE DISSERTATION

Electrical and Thermoelectrical Transport Properties
of Graphene

by

Deqi Wang

Doctor of Philosophy, Graduate Program in Physics
University of California, Riverside, August 2011
Dr. Jing Shi, Chairperson

Graphene is a newly discovered material. It has many excellent properties, which make the research of this new material very important not only for the fundamental physics but also for the application. This thesis is a summary of our study in the electrical and thermoelectrical transport properties of graphene. In the first part of our work, we use a layer of molecules act as the charge reservoir to control the charge environment near or on graphene, we first obtained a mobility enhancement. By set the charge back and forth between graphene and the molecules, we found the graphene mobility can be widely tuned from 4000 to 19000 cm^2/Vs. This strongly supports that charge impurities scattering is the main mechanism for graphene mobility. In addition, the charge neutral point in graphene can also be tuned independently over a wide gate voltage. A large

memory effect is also found in the graphene device addressed with molecules, which makes this system potentially important for graphene application, such as graphene FLASH memory. In the second part of our work, we studied the thermopower of graphene with a wide range of mobility, i. e. varying degree of disorders, along with electrical conductivity at different temperatures. We have proved that the transport properties in graphene are indeed caused by the Dirac fermions particles. Moreover, we have found that the Mott relation fails in the vicinity of the Dirac point in high-mobility graphene. By properly taking account of high-temperature effects, we have obtained good agreement between the Boltzmann transport theory and our experimental data. In low-mobility graphene where the charged impurities induce relatively high residual carrier density, the Mott relation holds at all gate voltages.

Table of Contents

List of Figures

List of Tables

Chapter I
Introduction

I-1 The Discovery of Graphene

Graphene is an isolated two-dimensional (2D) atomic plane of graphite. It is the base for other dimensional graphitic materials, such as 0D buckyball, 1D carbon nanotube, and 3D graphite (Figure I-1). Over several decades, graphene has been studied as a "theoretical material" for describing the properties of other carbon materials. The reason that people believed it only exists theoretically is that the thermal fluctuation in 2D crystal causes the lattice dislocations or defects at finite temperature to destabilize the crystal structure [Peierls, 1935, Landau, 1937]. In 2004, two physicists from University of Manchester successfully isolated the 2D carbon layer by mechanical exfoliation from graphite. Graphene, a new shining star, starts to shock the world by its brilliant properties. And a new era for condensed matter physics has begun.

The realization this 2D material is due to the strong carbon-carbon bonds in graphene, which keep the thermal fluctuations from destroying the crystal structure. In addition, the crumpling in the third dimension, i. e. the ripple, increases the

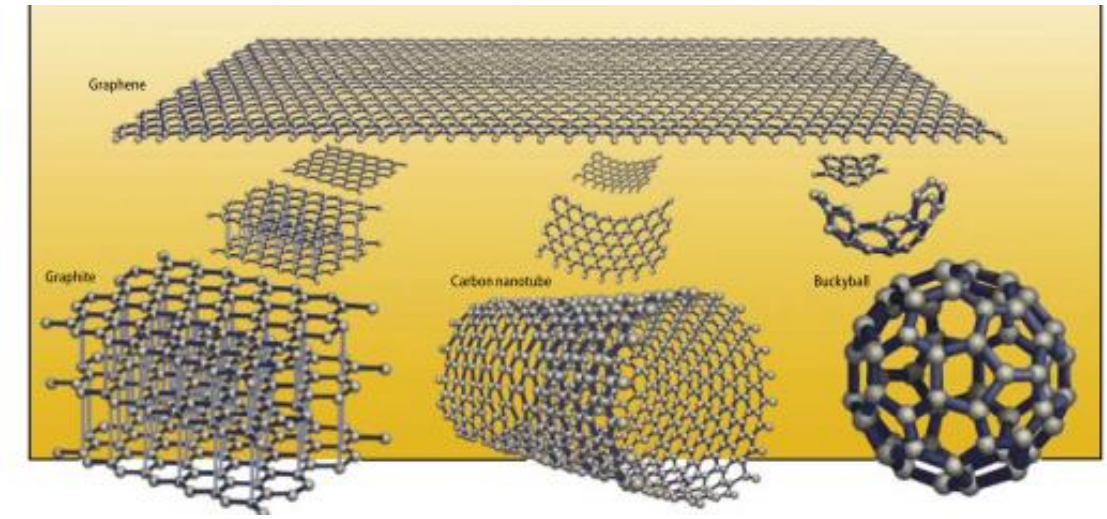

Figure I-1 Graphene is the base for other dimensional graphitic materials: 0D buckyball, 1D carbon nanotube and 3D graphite. [Geim, *et al.* 2008]

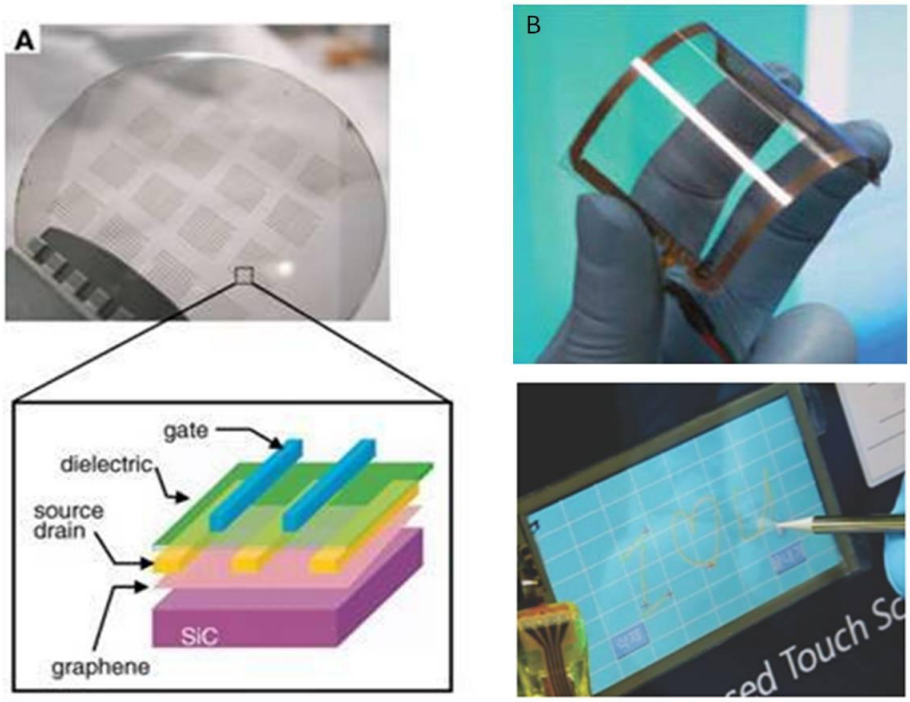

Figure I-2 (A) IBM demonstrated 100 Ghz graphene transistor (B) Samsung has made graphene touch screen

elastic energy in graphene which suppresses the thermal vibrations at finite temperature [Geim, *et al.,* 2007]. There are some other 2D materials obtained experimentally, such as one layer boron nitride, half-layer BSCCO [Novoselov *et al.,* 2005]. But none of them attracts as much attention as graphene does. For fundamental physics research, graphene provides a brand new system for the condensed matter physicists. It has unique electronic band structure, in which energy dispersion is linear at low energy, and the carrier in graphene is massless Dirac particle, which brings the quantum relativistic experiment to the table. For future applications, graphene has been believed to be a great candidate in different kinds of areas. For example, graphene has outstanding intrinsic carrier mobility and ultimate thickness, so it seems to be a good post-silicon material when now silicon based semiconductor technology almost reaches it fundamental limit. IBM has demonstrated 100 GHz transistor using large area graphene [Lin, *et al.,* 2010]. Graphene is optically transparent and is a good conductor for heat and electricity. Samsung has made touch screen by graphene [Bae, *et al.,* 2010] (Figure I-2). Graphene surface is very sensitive, so it can also be used for biosensor, and the sensitivity can be up to the single molecule level [Schedin, *et al.,* 2007].

There are several ways to obtain graphene, the physicists who discovered graphene used the so called “Drawing Method”, in which graphene is obtained by mechanical

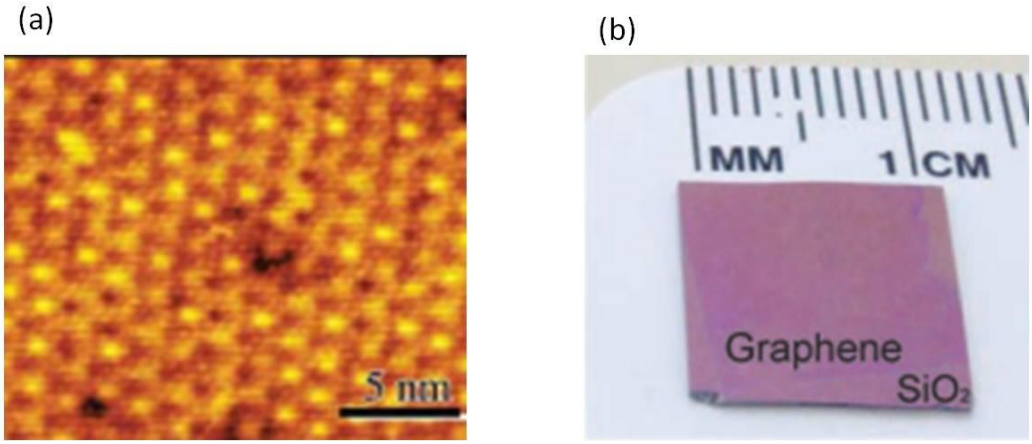

Figure I-3 (a) STM image of one monolayer of epitaxial graphene on SiC (b) CVD grown graphene transferred to SiO_2/Si substrate

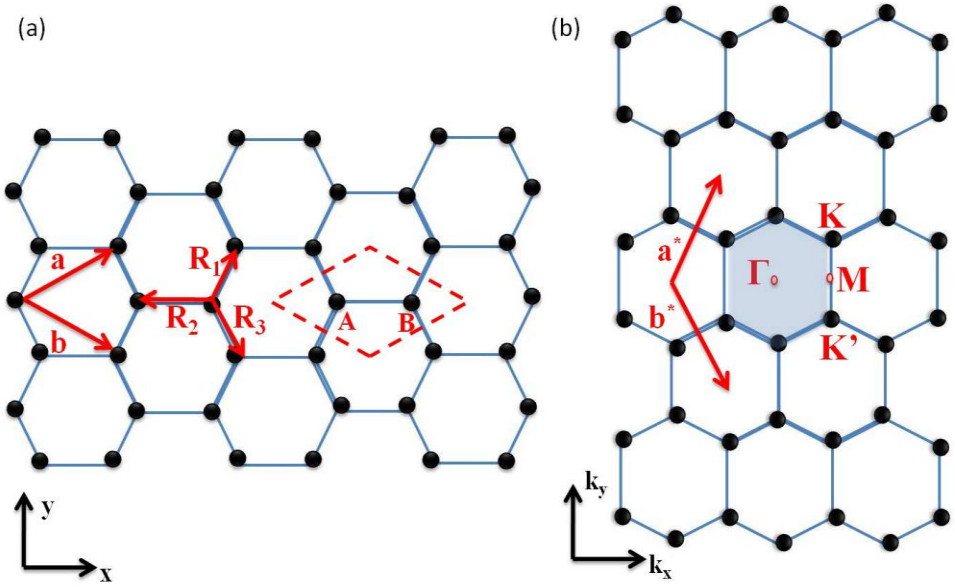

Figure I-4 (a) Graphene lattice in real space (b) Graphene lattice in reciprocal space.

exfoliation from graphite. One thing worth mentioning is the carefully selected substrate (300 nm SiO_2 on Si wafer) for graphene. If it were not for this magic substrate, we would not be able to see the small noticeable contrast for graphene with an optical microscope, and graphene would have probably remained undiscovered today. The drawing method is generally good for research purpose. For large-scale applications, graphene needs to be synthesized in large area. Now there are two methods for making large area grephene, one is the epitaxial growth of graphene on SiC substrate [Berger, *et al.*, 2006], and the other is the CVD growth on transition metals, such as Ni, Cu [Li, *et al.*, 2009] (Figure I-3). The latter seems to be more promising since the CVD grown graphene can be transferred to any arbitrary substrate. But the problem existing now is that quality of CVD grown graphene is still inferior to that from Drawing Method or epitaxial growth on SiC. The defects and impurities mostly come from the transferring process. The more advanced transferring technique is still under development.

I-2 Structure of Graphene

Graphene is a layer of carbon atoms arranged in the honeycomb lattice structure. The unit cell of lattice is the rhombus, which is indicated in dash line in Figure I-4 (a). The carbon-carbon distance a_{c-c} in graphene is 1.42 Å . There are two atoms A and B in

graphene unit cell. The real-space primitive vectors of the unit cell $\vec{a}$ and $\vec{b}$ are:

$$\vec{a} = (\frac{\sqrt{3}}{2}a, \frac{1}{2}a) \qquad \vec{b} = (\frac{\sqrt{3}}{2}a, -\frac{1}{2}a) \qquad (1)$$

where a is the lattice constant. It is equal to $\sqrt{3}a_{c-c} = 2.46\text{Å}$. The corresponding reciprocal lattice is shown in Figure I-4 (b), with the primitive vectors $\vec{a}^*$ and $\vec{b}^*$ given as:

$$\vec{a}^* = (\frac{2\pi}{\sqrt{3}a}, \frac{2\pi}{a}) \qquad \vec{b}^* = (\frac{2\pi}{\sqrt{3}a}, -\frac{2\pi}{a}) \qquad (2)$$

The lattice in reciprocal space is still hexagonal lattice with lattice constant equal to $\frac{4\pi}{3a}$. The shaded area in Figure I-4 (b) is the first Brillouin Zone. Among the high symmetry points (Γ, M, K, and K'), K and K' have another name called the Dirac Point, and their positions in momentum space can be written as:

$$K = \left(\frac{2\pi}{\sqrt{3}a}, \frac{2\pi}{3a}\right) \qquad K' = \left(\frac{2\pi}{\sqrt{3}a}, -\frac{2\pi}{3a}\right) \qquad (3)$$

K and K' are very important in graphene electronic properties. The reason will be discussed in the next section.

I-3 Energy Dispersion Relation of Graphene

The energy dispersion relation of graphene can be obtained by the tight binding method. In graphene lattice, each carbon A (B) atom has three nearest B (A) atoms, which

are denoted by $\vec{R}_1$, $\vec{R}_2$ and $\vec{R}_3$ in Figure I-4 (a), and six next nearest A (B) atoms. The nearest neighbor hopping energy t is about 2.8 eV while the next nearest neighbor hopping energy t' is found to be ~0.1 eV. Since t>>t', in the tight binding method, we only consider the nearest-neighbor interaction. The Hamiltonian matrix can be written as:

$$H = \begin{pmatrix} 0 & H_{AB} \\ H^*_{AB} & 0 \end{pmatrix} \qquad (4)$$

where H_{AB} is expressed as:

$$H_{AB} = t(e^{i\vec{k}\bullet\vec{R}_1} + e^{i\vec{k}\bullet\vec{R}_2} + e^{i\vec{k}\bullet\vec{R}_3}) = tf(\vec{k}) \qquad (5)$$

Then the energy bands solved from this Hamiltonian can be:

$$E_{\pm}(\vec{k}) = \pm t\sqrt{3 + f(\vec{k})} \qquad (6)$$

where $f(\vec{k})$ is the sum of phase factor $e^{i\vec{k}\bullet\vec{R}_i}$, it can be expressed as:

$$f(\vec{k}) = 2\cos(ak_y) + 4\cos(\frac{a}{2}k_y)\cos(\frac{\sqrt{3}a}{2}k_x)\,. \qquad (7)$$

The plus sign in $E_{\pm}(\vec{k})$ applies to the upper π^* band and the minus sign applies to the lower π band. $E_{\pm}(\vec{k})$ is equal to zero at K and K'. At low energies, by expanding $E_{\pm}(\vec{k})$ near K (or K'), we can obtain:

$$E_{\pm}(\vec{k}_0) = \pm\hbar v_F \vec{k}_0 \qquad (8)$$

where $\vec{k} = K(K') + \vec{k}_0$ ($|\vec{k}_0| << |\vec{K}(\vec{K}')|$) is applied. v_F is called the Fermi velocity and

$$v_F = \frac{\sqrt{3}at}{2\hbar} = 1\times10^6 m/s\,. \qquad (9)$$

Comparing Equation (8) with the energy dispersion in other 2D electron gas system, which is given as $E(\vec{k}) = \frac{\hbar^2 \vec{k}^2}{2m}$, we can see that the carrier in graphene is massless with linear energy dispersion which can be described by the Dirac Equation with the speed of light replaced by the Fermi velocity v_F. This is why K and K' point are called the Dirac Points. The "$\pm$" in Equation (8) refers to the conduction and valence bands which meet at the Dirac Points ($\vec{k}_0 = 0$), with no energy gap separating the two. Graphene is thus a zero band gap semiconductor. Figure I-5 is a 3D plot of graphene energy relation. The corners of the hexagonal Brillouin Zone correspond to six Dirac Points (K and K') [Wilson, 2006].

Graphene's unique linear energy dispersion and Dirac fermion nature have been proved by the quantum Hall effect with half integer quantized Hall conductivity, i. e. $\sigma_{xy} = \pm 4e^2 / h(N + 1/2)$, where N is the Laudau level index and factor 4 is due to double valley and double spin degeneracy [Novoselove, *et al.*, 2005, Zhang, *et al.*, 2005]. In our work, we use thermopower as a sensitive tool to probe the transport properties in graphene. Our results support the transport in graphene is indeed caused by the massless Dirac particle, which is another piece of strong experimental evidence for the unique graphene electronic spectrum.

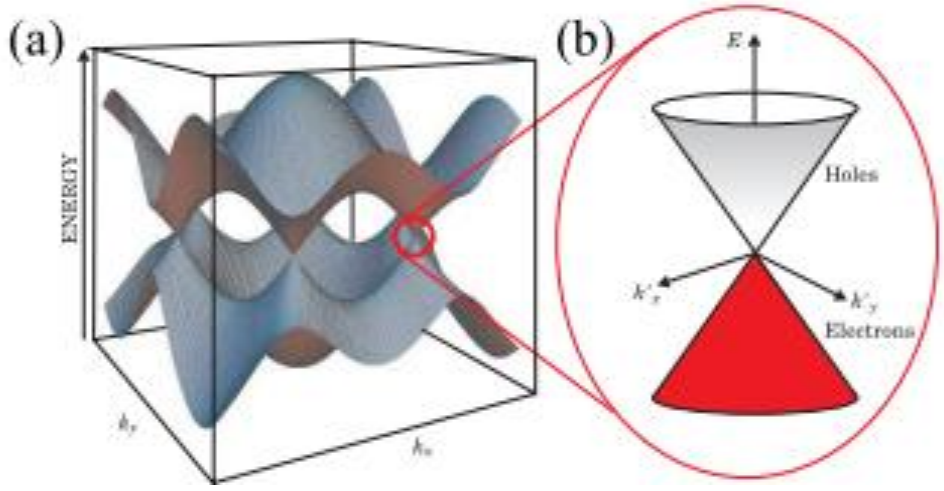

Figure I-5 (a) Graphene band structure (b) Enlarged band structure closed to K (K') point [Wilson, et al. 2006]

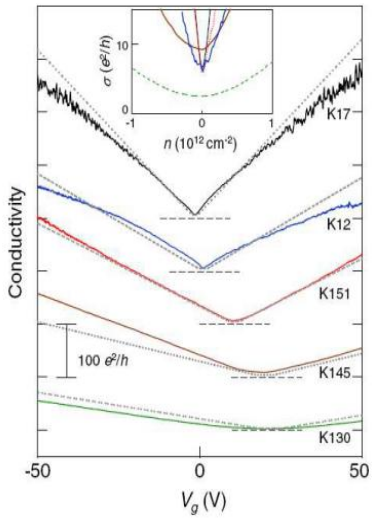

Figure I-6 The conductivity of five representative samples as a function of applied gate voltage. For clarity, curves are vertically displaced. The horizontal dashed lines indicate the zero conductance for each curve. Dotted curves are the corresponding theoretical fits. The inset shows the detailed view of the density-dependent conductivity near the Dirac point for the data in the main panel [Tan et al. 2007].

I-4 Scattering Mechanism for Graphene Mobility

Graphene has always attracted physicists by its excellent electronic properties. The large carrier mobility makes graphene an enticing material for novel electronic applications. The sigma bonding in graphene is so robust that it is difficult for other atoms to replace the carbon atoms in the honeycomb lattice. This is one of the reasons that graphene has a long mean-free-path, which can be up to 1 μm. However, graphene is not immune to disorders and its electronic properties are controlled by both the extrinsic or intrinsic disorders, which limit the graphene mobility at different levels.

The extrinsic disorders include the vacancies, adatoms, and charges on top of graphene or in the substrate. Among them, the long range Coulomb charge disorders are believed to be the dominant scattering sources for graphene mobility [Das Sarma, *et al.* 2011]. The charge impurity model can explain recent transport experiments very well. Tan *et al.* (2007) have found that the correlation of the sample mobility with the shift of the Dirac point and the minimum conductivity plateau width, showing qualitative and semi-quantitative agreement with the calculations with long-range Coulomb disorders [Figure I-6]. Chen *et al.* (2008) studied the effect of the long-range charge impurities on graphene conductivity and mobility by intentionally depositing potassium ions

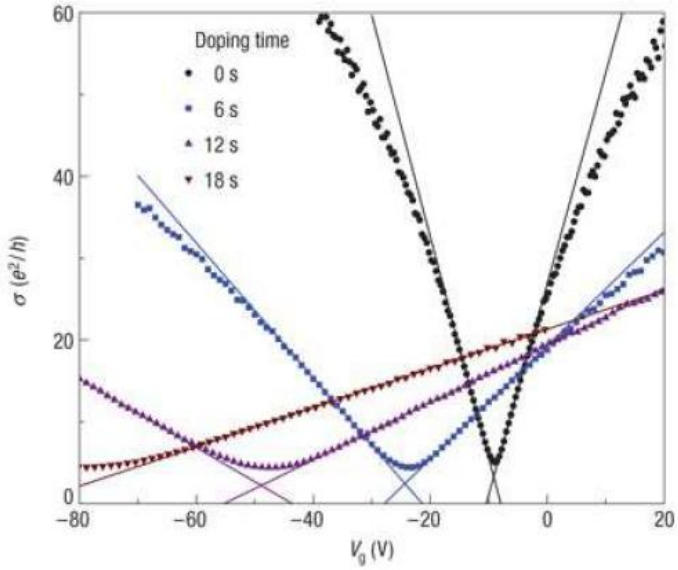

Figure I-7 The conductivity versus gate voltage curves for the pristine sample and three different doping con-centrations. Lines are theoretical calculation, and the crossing of the lines defines the points of the residual conductivity and the gate voltage at minimum conductivity for each data set [Chen et al. 2008]

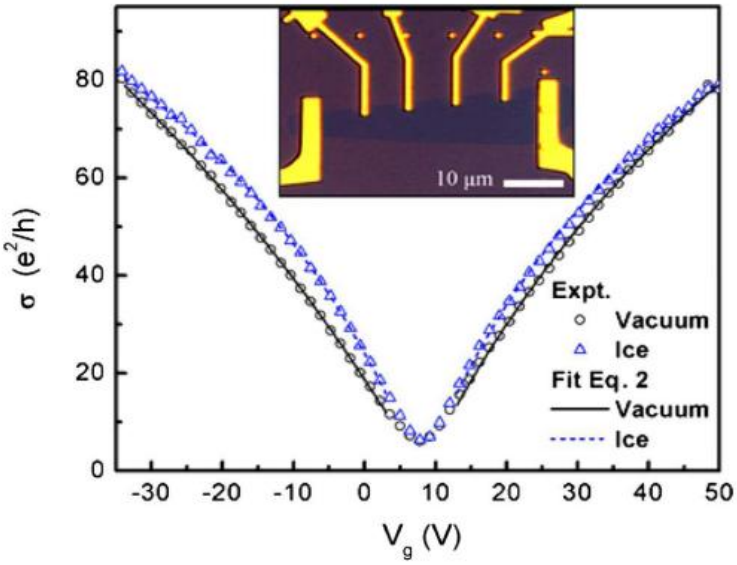

Figure I-8 Conductivity of the graphene device as a function of back gate voltage for pristine graphene (circles) and after deposition of 6 monolayers of ice (triangles). Lines are theoretical results. Inset: Optical microscope image of the device [Jang et al. 2008].

on graphene in ultra-high vacuum [Figure I-7]. The observed phenomena qualitatively agree with the Coulomb charge impurity model. Jang *et al.* (2008) have found the graphene mobility enhancement by depositing ice on top of graphene [Figure I-8], which is predicted by the Boltzmann theory with Coulomb disorders. Bolotin, et al. (2008) and Du et al. (2008) got dramatically improved graphene mobility in suspended graphene devices by removing the SiO_2 substrate [Figure I-9]. This again confirms (or strongly supports) the remote charge scattering in graphene. For extrinsic disorders, the remote interface polar optical phonon in the substrate is also considered [Chen, *et al.*, 2008]. Higher mobility is indeed obtained in using other substrate such as Boron Nitride [Dean, *et al.*, 2010].

Although the extrinsic disorders play an important role in graphene mobility, the scattering from intrinsic disorders cannot be ignored. Graphene is not a perfect atomically 2D sheet; it is the extreme case of a soft membrane. So it is subject to distortions of its structure due to thermal fluctuations or interaction with a substrate. When placed on a substrate, graphene will conform to the surface roughness developing ripples. Ripples are inherent features of graphene and they may also create a long-range scattering potential in graphene to limit the mobility [Katsnelson *et al.*, 2008]. Ponomarenko, *et al.*, (2009) have found no significant change in graphene mobility when their devices are made with

different substrate or high dielectric media. So they claimed that Coulomb impurities may not be the dominant scattering for graphene while scattering from ripples or other resonant scatterers might be the main mechanism. Besides ripples, other intrinsic scattering sources such as the longitudinal acoustic phonons scattering, are also considered. [Das Sarma, *et al.*, 2011, Chen, *et al.*, 2008].

If all the charge impurities are removed in graphene, the remote interfacial phonon scattering will limit the room temperature mobility to $4\times10^4 cm^2V^{-1}s^{-1}$. And if the remote interfacial phonon scattering is removed from graphene, the intrinsic longitudinal acoustic phonons scattering will limit the mobility to $2\times10^5 cm^2V^{-1}s^{-1}$. These two numbers do match with the experimental results.

In our work, first of all, by changing the charge state of graphene, we obtained different graphene mobility, which provides direct evidence for the charge impurity scattering mechanism in graphene. Secondly, using thermopower as a tool, we find a good agreement between our experimental data and the theory when the charge impurity model is applied, which is also another piece of strong evidence for the validity of this model.

I-5 Charge Impurity Model

The presence of charge impurities in graphene degrade the carrier mobility and chemically dope the graphene, shifting the Fermi level away from Dirac Point, which results in a non-zero Dirac point gate voltage in the experimental σ vs V_g plot. In addition, charge impurities provide an inhomogeneous electron-hole puddle landscape at low carrier density close to the Dirac Point, which makes the conductivity approximately a constant over a finite range of external gate voltage, which is observed as the minimum conductivity plateau in experimental σ vs V_g plot. Adam, *et al.*, (2007) used the full random phase approximation-Boltzmann formalism to investigate the charged impurity scattering in graphene, and they found that most of the observed transport properties of graphene sheet at zero magnetic field can be explained. The result can be expressed as:

$$\sigma\left(n-\bar{n}\right)=\begin{cases}\dfrac{20e^2n^*}{hn_{imp}} & \text{if } n-\bar{n}<n^{I*}\\ \dfrac{20e^2n}{hn_{imp}} & \text{if } n-\bar{n}>n*\end{cases} \qquad (10)$$

$$\mu=5\times10^{15}/n_{imp} \qquad (11)$$

σ : Graphene conductivity

n_{imp} : Density of charge impurities

n^* : Carrier density fluctuation (residue carrier density) near Dirac point caused by the charge impurities

$\bar{n}$: Carrier density shifted by the chemical doping of charge impurities

μ : Carrier mobility

Using this model, one can calculate n_{imp} and n^* by using measured σ and μ. We will use this model to analyze our thermopower data.

I-6 Thermoelectric Power or Thermopower

When a heat flow is applied through a conductor, one can observe an electric voltage generated between the two ends of the conductor. At the atomic scale, the applied temperature gradient causes charged carriers in the material to diffuse from the hot side to the cold side, similar to a classical gas that expands when heated; hence inducing an electric field or a voltage, so we call this the thermoelectric effect. This effect is characterized by the Seebeck coefficient or thermopower defined as:

$$S = -\frac{\Delta V}{\Delta T}, \qquad (12)$$

where ΔV is the generated thermal voltage and ΔT is the temperature difference between hot and cold ends.

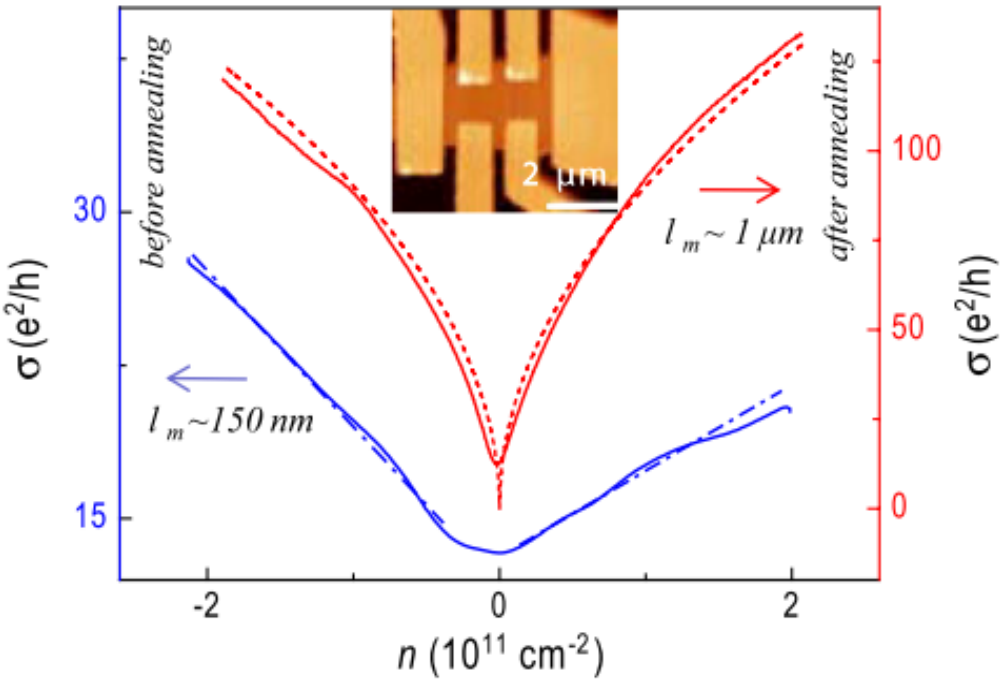

Figure I-9 Conductance of the suspended graphene sample before [lower (blue) line] and after [upper (red) line] annealing as a function of carrier density. Data are shown for T = 40 K to suppress mesoscopic conductance fluctuations. Note the change from near-linear to sublinear behavior before and after annealing, respectively. The dotted upper (red) line is the expectation for ballistic transport (see text). Inset: Atomic force microscope image of the suspended device. [Bolotin, et al., 2008]

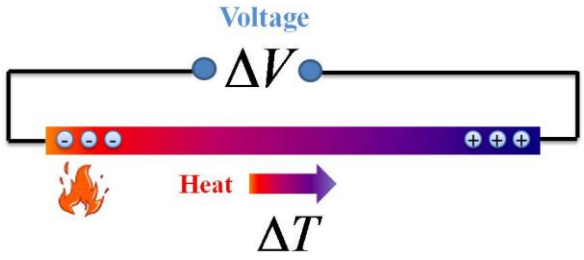

$$S = -\frac{\Delta V}{\Delta T}$$

Figure I-10 The definition of thermopower or the Seebeck coefficient

Since thermoelectric power is the conversion between the thermal energy and electricity, materials with large thermopower have potential applications for power generation or refrigeration. Also, another simple and well-known application of the thermoelectric transport is thermocouples, which use the output thermal voltage and pre-calibrated thermopower of the thermalcouples to monitor the temperature. In condensed matter physics, thermoelectric transport coefficients could be tightly connected with their counterparts in electrical transport through famous Mott's relation which is mathematically derived from Boltzmann's transport equations under the relaxation time or scattering rate approximation.

$$S = -\frac{\pi^2 k_B^2 T}{3e}\left(\frac{\partial \ln \sigma(\mu)}{\partial \mu}\right) \qquad (13)$$

where k_B is the Boltzmann constant, σ is conductivity, and μ is the chemical potential. From the Mott relation, we can see that thermopower can provide more information about the materials than the electrical conductivity. First of all, the type of carriers can be determined from the sign of the thermopower. Electron conduction gives a negative S while hole conduction gives a positive S. In addition, since S is proportional to the derivative of the conductivity with respect to the energy at Fermi level, it is very sensitive to the electronic properties such as the density-of-states near the Fermi level and the scattering mechanism. One can study the mechanism of scattering from the temperature

dependence of thermopower. In our work, we use themopower as a sensitive tool to study the new material, graphene. By investigating the thermoelectric transport, we have learned a lot of information about the electronic band structure and the electron scattering mechanism in graphene.

Reference:

Peierls, R. E., Ann. I. H. Poincare 1935, 5, 177-222

Landau, L. D., Phys. Z. Sowjetunion 1937, 11, 26-35

Geim, A. K., *et al.*, Nature Materials 2007, 6, 183-190

Novoselov, K. S., *et al.*, Proc. Natl. Acad. Sci. 2005, 102, 10451-10453

Lin, Y. M., *et al.*, Science 2010, 327, 6

Bae, S. K., *et al.*, Nature Nanotechnology 2010, 5, 574-578

Schedin, F., *et al.*, Nature Materials 2007, 6, 652 – 655

Berger, C., *et al.*, Science 2006, 312, 1191

Li, X. S., *et al.*, Science 2009, 324, 1312

Wilson, M., Physics Today 2006, 59, 21-23

Novoselove, K. S. *et al.*, Nature 2005, 438, 197-200

Zhang, Y. B., *et al.*, Nature 2005, 438, 201-204

Das Sarma, S., et al., Rev. Mod. Phys. 2011, 83, 407-470

Tan, Y. W., *et al.*, Phys. Rev. Lett. 2007, 99, 246803

Chen, J. H. *et al.*, Nat. Phys. 2008, 4, 377-381

Jang, C. *et al.*, Phys. Rev. Lett. 2008, 101, 146805

Bolotin, K. I. *et al.*, Phys. Rev. Lett. 2008, 101, 096802

Du., X., *et al.*, Nat. Nano. 2008, 3, 491-495

Katsnelson, M. I., *et al.*, Phil. Trans. R. Soc. 2008, 366, 195-204

Chen, J. H. *et al.*, Nat. Nano. 2008, 3, 206-209

Chapter II
Fabrication of Graphene Devices and Experimental Setup

II-1 Exfoliation of Graphene From Graphite

In this thesis, all the graphene devices are made from the exfoliated flakes from either the highly ordered pyrolytic graphite (HOPG) or Kish graphite. Figure II-1 (a) and (b) show pictures of HOPG and Kish graphite. To get the graphene piece, the "Drawing Method" was used, which is first demonstrated by Novoselov *et al.* in 2004.

First of all, the substrate wafers should be prepared. The substrate is a 300 nm SiO_2 layer thermally grown on highly doped 0.8 (? Typically 0.5)-mm-thick silicon substrate. The 4-inch wafers are commercially available from University Wafer and cut into 5 mm × 5 mm chips by the milling machine in the clean room of University of California, Irvine. To clean the chips, we first dip them in the 80 ^{o}C acetone for 30 minutes and then transfer to room temperature IPA and DI water for 10 minutes respectively. Afterwards H_2O_2 solution is used. We put the chips in the H_2O_2 solution for 20 minutes and wash them in the DI water again for 5 minutes. All the chips are next transferred to the Rapid

(a)

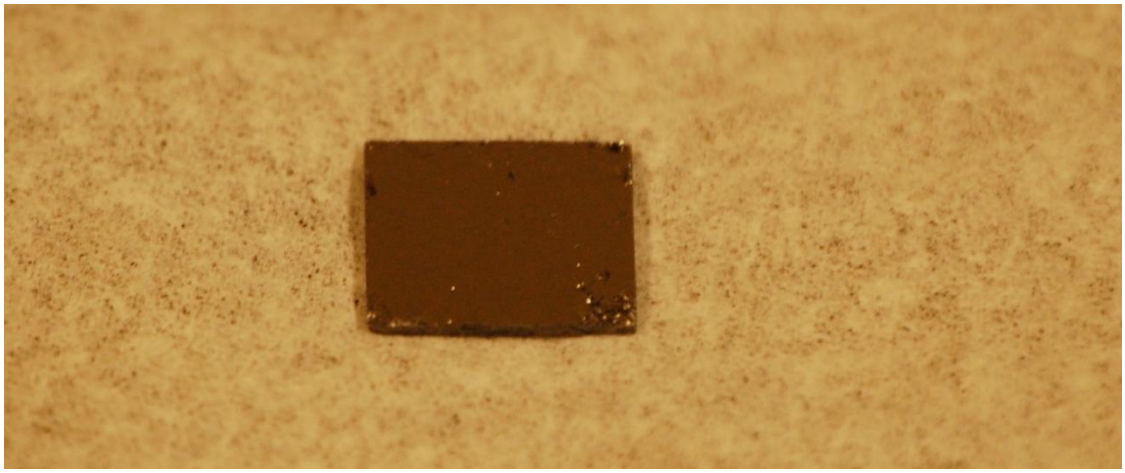

(b)

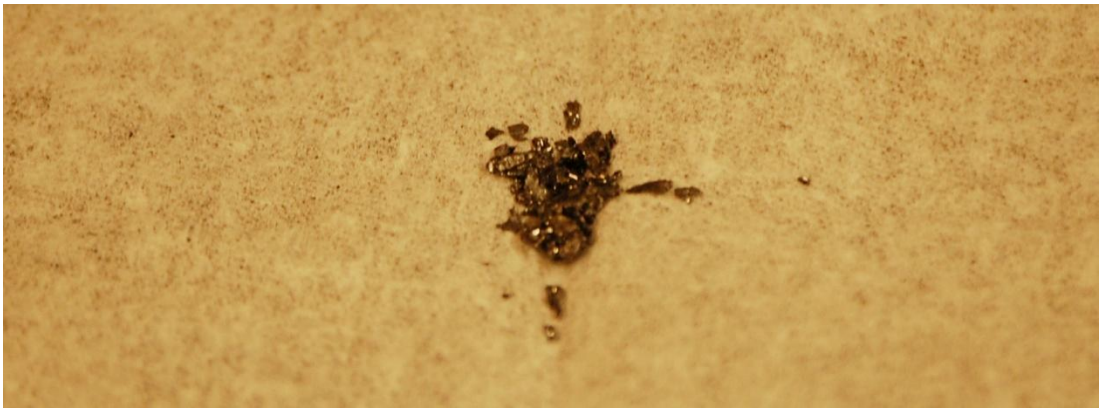

Figure II-1 Image of HOPG (a) and Kish Graphite (b)

Thermal Annealing System (RTA) to do the annealing at 200 ^{o}C in the Argon gas atmosphere for 30 minutes. Finally, a Reactive Ion Etching (RIE) O_2 plasma cleaning on the chips is performed. This finishes the preparation of the substrate.

To get a graphene flake, in the first place, obtain a 15-cm long Scotch tape and gently lay it down on a flat surface with the adhesive side facing up. Use a clean tweezers to take HOPG or a piece of thin Kish graphite and place it onto the adhesive side of the Scotch tape. For HOPG, now use a plastic tweezers to press the surface softly, and then take the whole HOGP off. There will be a thin HOPG flake left on the tape. For Kish graphite, this step can be skipped. Secondly, fold the Scotch tape at the edge of the graphite flake and peel it off gently. Do this step several times until you obtain a newly transparent region on the Scotch tape. Finally, take a clean SiO_2 substrate chip and put the Scotch tape on top of the chip. Press the tape gently using a plastic tape and peel off the tape slowly. The chip is then transferred to Nikon Eclipse LV150 optical microscope to look for the graphene. The graphene will be shown as the purple spot in the optical microscope. Figure II-2 displays the process of "Drawing Method". Using this method, usually graphene got from HOPG is shorter and narrower than from the Kish graphite. Figure II-3 shows an optical image of single layer graphene, double layer graphene, multilayer graphene and graphite. There are some tape residues left on the substrate.

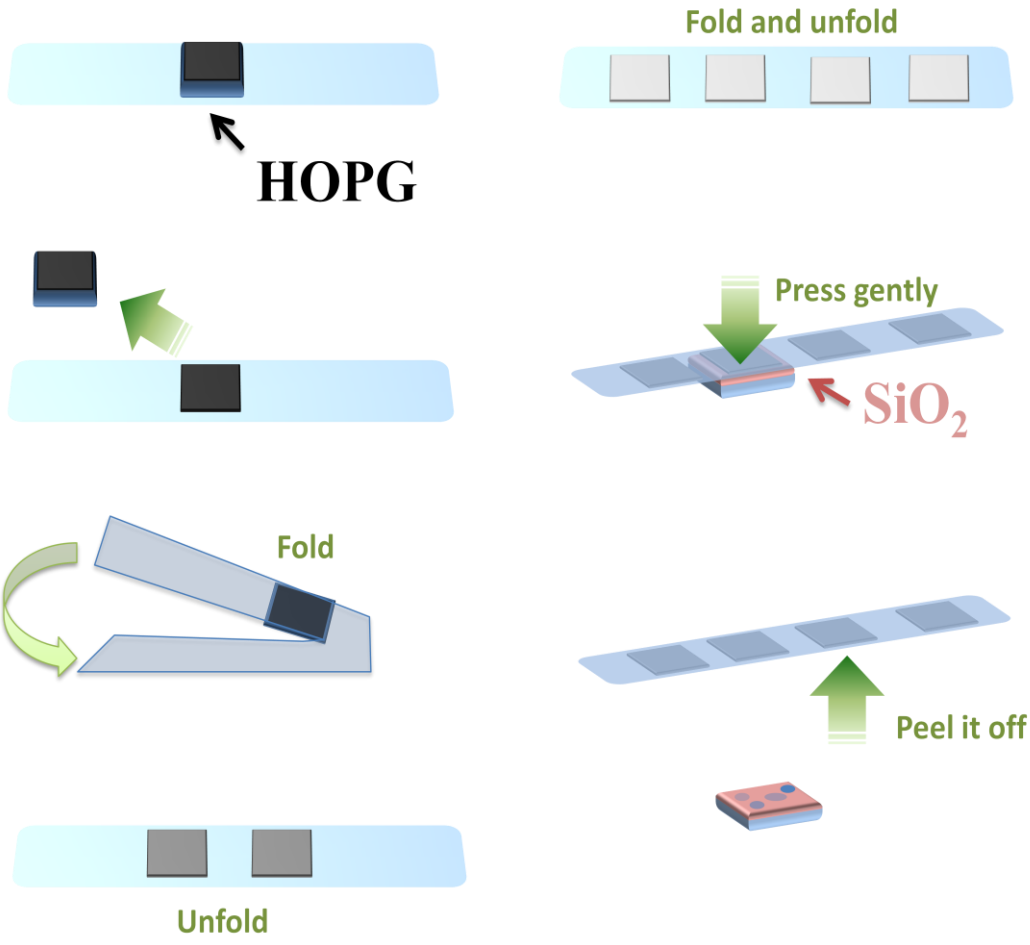

Fig. II-2 Obtain graphene by using Drawing Method on HOPG

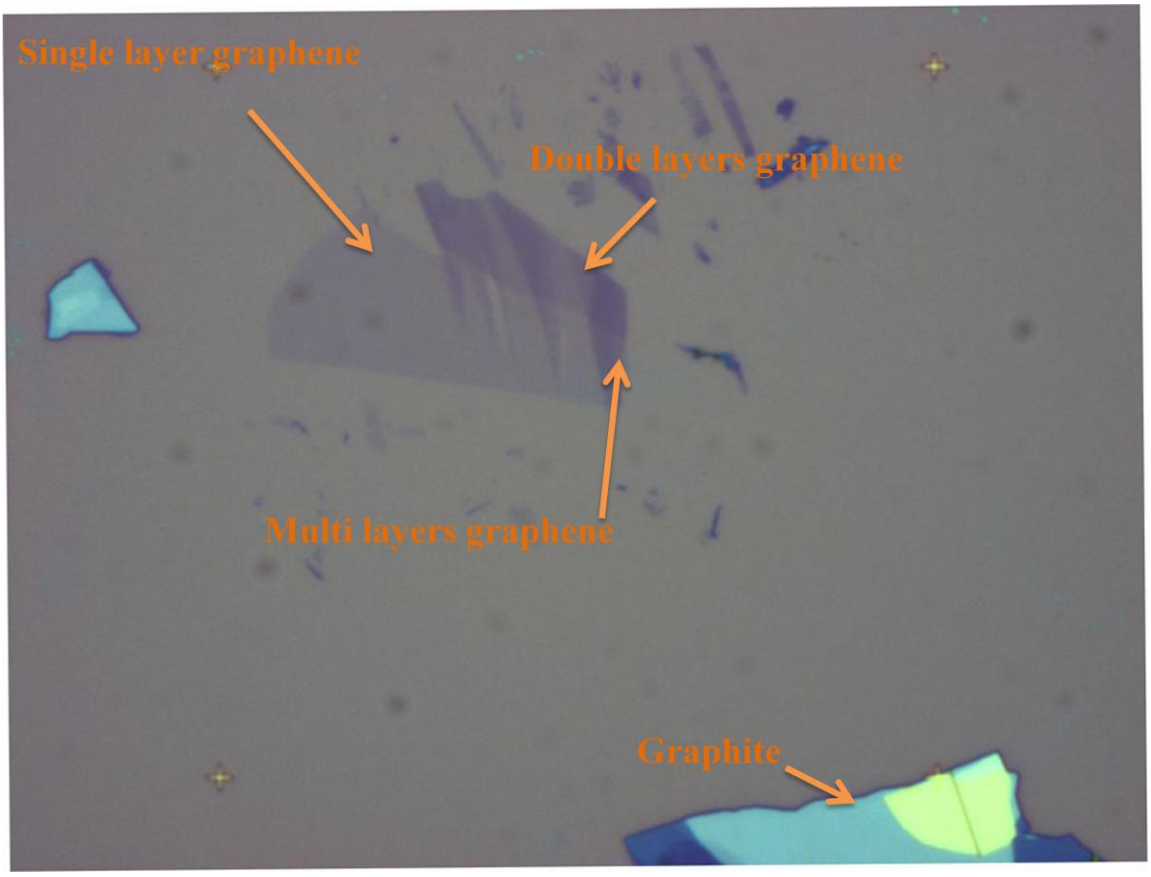

Figure II-3 An optical image of single layer graphene, double layer graphene, multi layers graphene, and graphite.

They can be removed by doing oxygen annealing in the furnace at 300 ^{o}C for an hour. However, this annealing may give a high doping to the graphene. So as long as the selected graphene area is clean to make the device. No annealing is needed.

II-2 Graphene Field Effect Transistor Devices and Thermopower Device Fabrication

II-2-1 Electron-beam lithography

After the graphene is transferred to the SiO_2 substrate, electron-beam lithography is used to make the pattern on the sample. We used double layer resist of methyl methacylate (MMA) and poly methyl methacrylate (PMMA). The MMA is first spin coated on the sample at the 3200 RPM for 45 seconds and then baked on the hot plate at 170 ^{o}C for 20 minutes. Then after the sample is cool, another layer of PMMA is spin coated at the same speed and baked at the same temperature and time. The total thickness of the two resist layer is about 500 nm. The electron beam exposure is done in the SEM system. The beam voltage is 20 kV. For small features, 20-μm aperture is used, and the beam current is set to 90 pA and the area dose is 500. While for large features, 120-μm aperture is used, the beam current is set to 2500 pA and the area dose is 450. After the exposure, the sample is developed in the mixed solvent (1:3) of Methyl isobutyl ketone

(MIBK) and Isopropanol (IPA) for 65 s. MMA dissolves faster than PMMA in the solvent, so we will have the undercut structure [Figure II-4]. Electron beam metal evaporation is performed after the developing. 10 nm Ti is first deposited followed by 50 nm (for alignment marks) or 80 nm (for electrode) Au. Finally the lift-off is done in the 80 ^{o}C acetone for 15 minutes, followed by the IPA wash. The undercut structure formed in the lithography helps produce clean edges of the metal in the lift-off.

II-2-2 Alignment Marks

In order to locate the graphene accurately on the substrate, alignment marks need to be made on the substrate first. The alignment mark pattern is edited and designed using NPGS and Design CAD. It is a matrix consisting of numerous ordered crosses with 60 μm spacing. The size of the cross is 2μm ×2μm and the total area of alignment mark pattern is 1.2 mm × 1.2 mm. After the graphene is selected from the optical microscope, the locations of graphene should be noted down roughly such as top left area or bottom right area of the substrate and marked by a droplet of silver paint. When writing a pattern in the SEM, find the silver paint on the sample and expose that area. After the alignment marks fabricated on the substrate, graphene and the gold alignment marks are taken

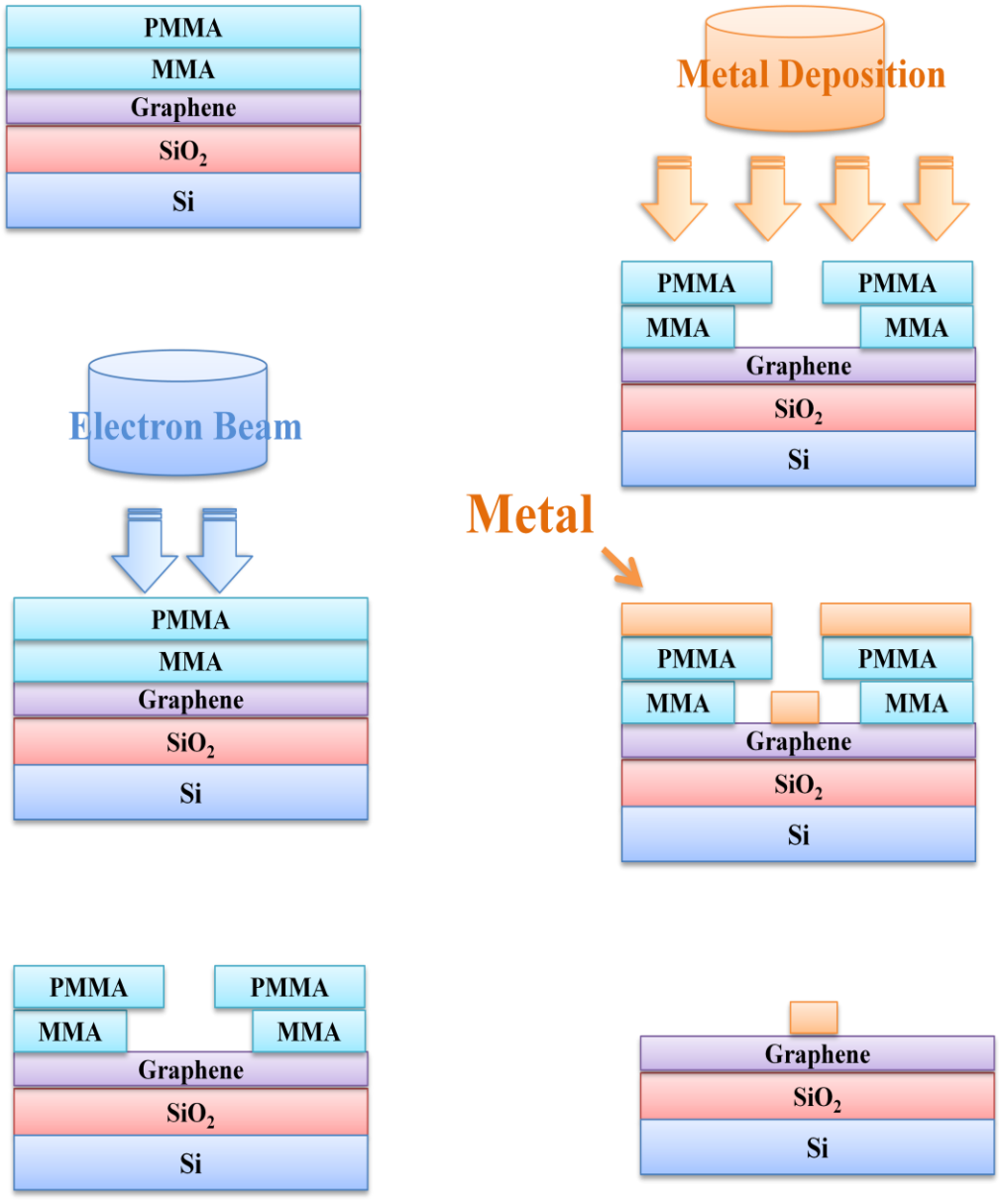

Figure II-4 Electron beam lithography, metal deposition and lift-off

pictures again in the optical microscope. Using the ordered numbers in the alignment marks and the NPGS alignment window, we can easily locate graphene on the substrate in the next lithography step.

II-2-3 Graphene Field Effect Transistor and Thermopower Device Structure

The graphene and alignment mark images are loaded into the DesignCAD to design the pattern for the electrodes. Depending on the size of the graphene flakes, the width of the electrodes can vary from 500 nm to 2 μm. For a regular graphene field effect transistor device, four electrodes are fabricated. If the Hall measurement is needed, two more Hall leads will be added to the device. RIE oxygen plasma can be used to etch the graphene if some particular shapes are required. For the thermopower devices, the device geometry is different. Two more thermometers and one heater are added. Figure II-4 (d) displays an optical image of a graphene thermopower device. 2 and 3 are two thermometers. Each of these two thermometers are connected to 4 wires, so that their resistance can be measured accurately. 5 is the heater, which is fabricated as closed as possible to electrode 4 to generate a temperature gradient efficiently. The distance usually varies from 300 nm to 1 μm in our devices. In order to get a uniform thermal distribution perpendicular to the channel (or along the thermometer electrodes), the length of the heater is designed to be at least 3 times of the thermometers.

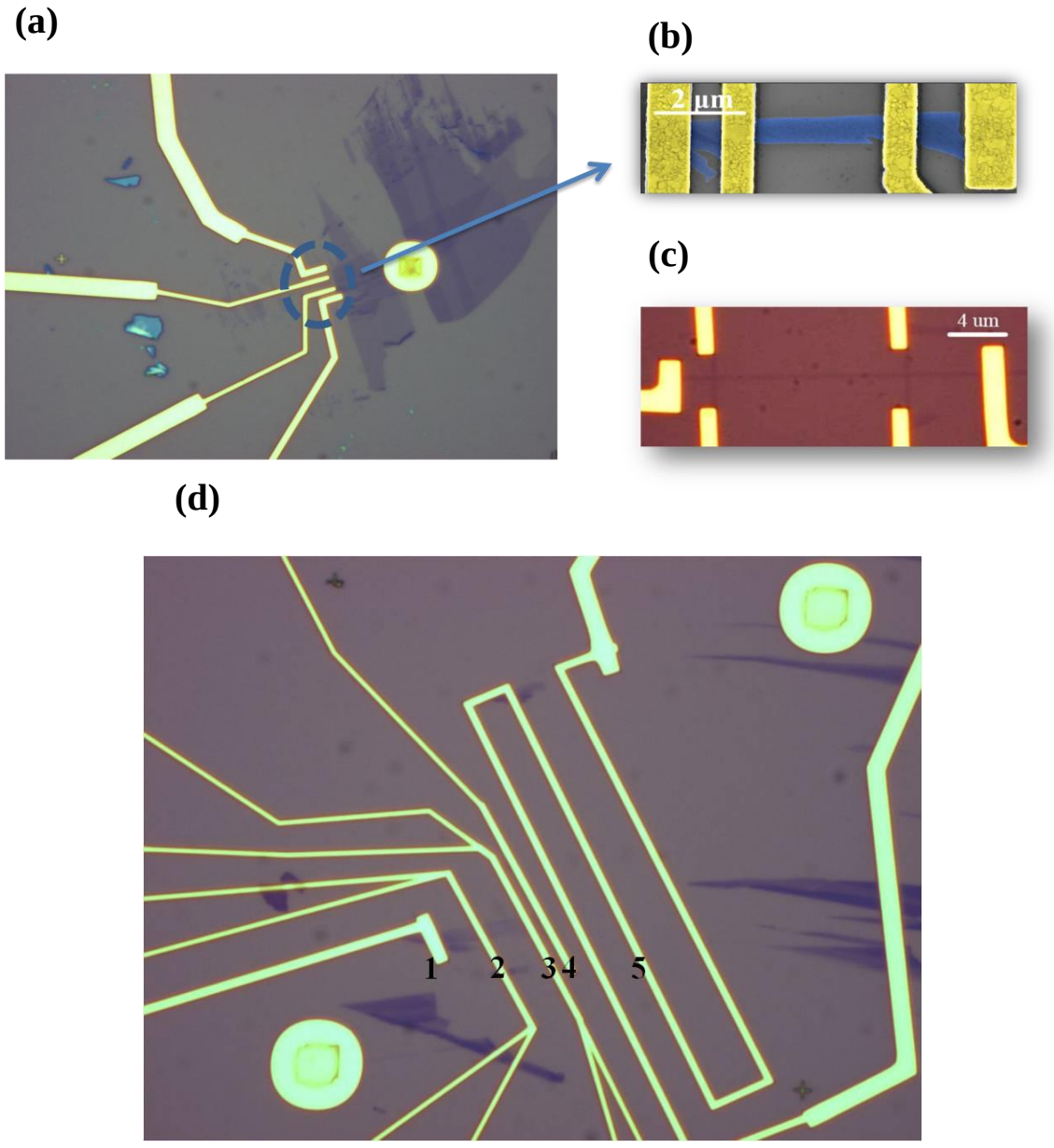

Figure II-5 (a). Optical image of graphene field effect transistor (b). False color SEM image of graphene field effect transistor (c). Optical image of etched graphene hall bar device (d). Optical image of graphene thermopower device

II-3 Measurement Setup

II-3-1 Continuous Flow Cryostat and Sample Mounting

All the measurements shown in this thesis are performed in a Continuous Flow Cryostat. This system consists of Janis Liquid Helium Transfer Line, Janis Cryostat, GMW Electron Magnet, Varian Turbo Pumping Station, and Homemade Stage. The chamber can be pumped to the pressure of 10^{-7} Torr. Liquid helium is used for cooling in this system, so the temperature can be varied from 4 K to room temperature, and it is controlled by Lake shore 330 Temperature Controller. The transfer line is designed to fit the 60 Liter liquid helium tank. Figure II-6 (a) displays a scheme of a similiar chamber from Janis Research website and (b) is the scheme of the sample holder, which can be taken apart from the system to do the wire bonding. There are 14 copper pins on the sample holder. They are connected to two Bayonet Neill-Concelman (BNC) cable boxes. The wiring of the system was first completed by Yong Pu and then modified by me to make it suitable for wire bonding.

In order to gate the device, a small piece of 1-mm-thick Al_2O_3 sheet is first glued to the sample holder with a 200-μm-thick copper sheet on top.

(a)

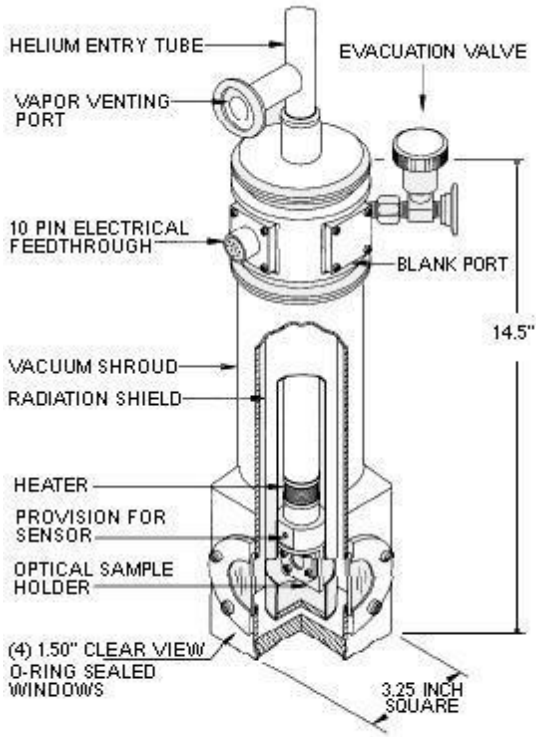

(b)

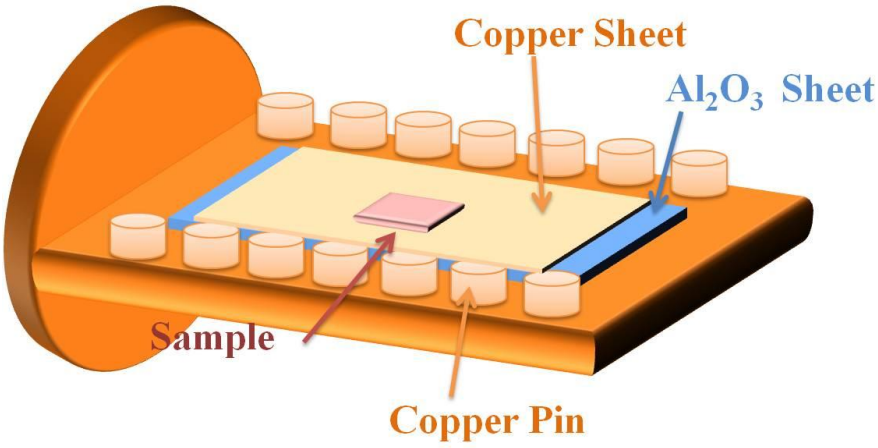

Figure II-6 (a) Scheme of a similar chamber from Janis Research website. (b) Scheme of the sample holder.

To measure the devices, the chips are first glued to the thin copper sheet by silver paint and wait 20 minutes for the silver paint to dry. Then WEST BOND system is used to do the wire bonding, connecting the copper pins on the sample holder to the bonding pads on the devices. For the gate pin, it is connected to the thin copper sheet instead. To protect the bonding pads and the graphene on the devices, generally the first bond will be applied on the sample holder with 300 ultrasonic power and 30 ms time, and then the wire is grounded. The second one is on the devices with 175 ultrasonic power and 30 ms time. The power used on the devices should be kept small enough not to damage the SiO_2 underneath; otherwise, the devices would have gate leakage.

II-3-2 Measurement Circuit Setup

To set up the measurement circuit, the meters are connected to those two BNC boxes, which are linked to the device. All the meters in the circuit are remotely controlled by a Nation Instrument Labview program. The measurement circuits for the electrical and the thermoelectric signals are different.

Figure II-7 (a) is a schematic diagram of the electrical measurement circuit. For the electrical measurements, in order to get a low noise to signal ratio, we use a Stanford

Research Systems 830 (SR 830) lock-in amplifier. A 14.97 MΩ resistor is connected in series to the SR 830 before it goes to the device, converting the voltage source to a current source. The current in the circuit is usually kept as small as several hundreds nano amperes. The frequency of SR 830 is set to 27.73 Hz to avoid any capacitance signal mixing and voltage signal from the device is sent back to SR 830 using the "A-B" input. Keithley 2400 SourceMeter (K2400) is used to apply the back gate voltage. A RC (R=1 MΩ, C= 20 nF) filter is used between K2400 and the device. If we connect K2400 directly to the device, due to the small capacitance of the device, the ramping voltage of K2400 (usually 0.2 V/s) would result in a rapid high current pulse on the device, which may cause damage. With the help of the RC filter, however, the time constant of the system is sufficiently large, so that the current pulses on the device are relatively low, and the device can be well protected.

For thermoelectric measurement setup, which is shown in Figure II-7 (a), is a little bit different. We used the same circuit setup to apply the back gate voltage as we do in the electrical measurements. But for the heater current in the device, it is applied by another K 2400 or Keithley 6221 current source. The thermal voltage generated from the device is usually very small. At low temperatures, it can be at the sub-micron volt level.

(a)

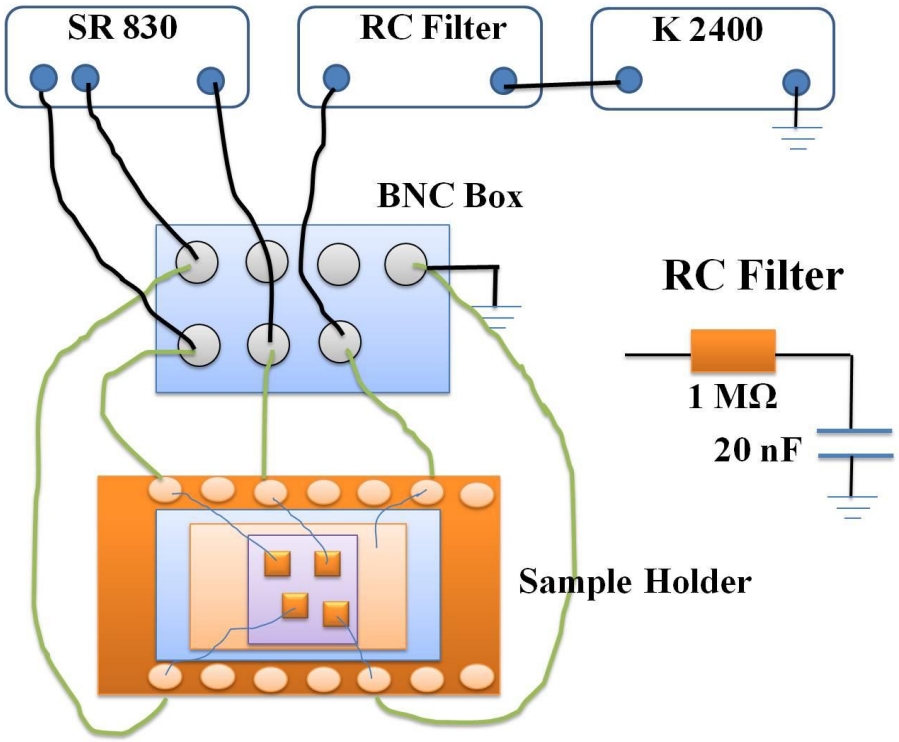

(b)

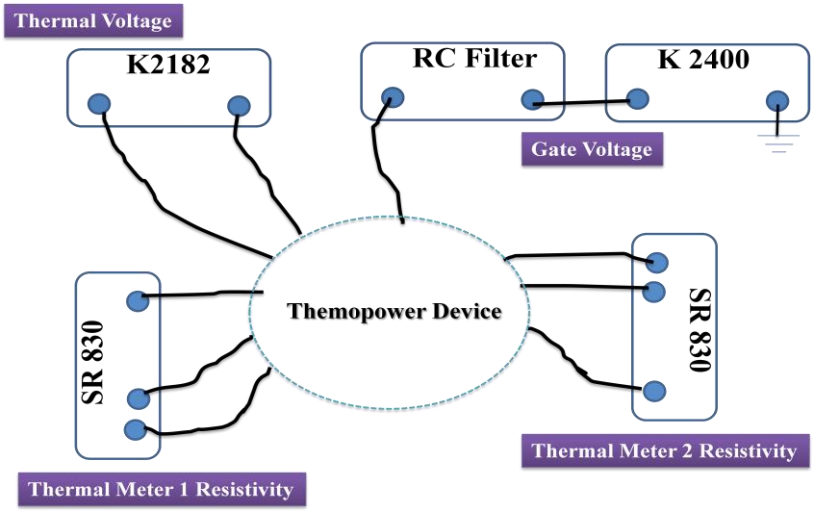

Figure II-7 Circuits set up of electrical measurement (a) and thermal electrical measurement (b)

So we used Keithley 2182 Nanovoltmeter (K2182) to detect the small voltages. Since there is always a thermal voltage background signal coming from the system, to detect the accurate thermal voltage generated by the heater, at each point, we measure the signal by subtracting the heater-off signal from the heater-on signal. The heater current is ramped to the set value at 1 mA / s. At the same time, the resistance of the thermometers is measured by two lock-in amplifiers simultaneously using different frequencies.

II-3-3 Continuous Flow Cryostat System Cooling

To cool down the system, a 60 liter liquid helium tank is usually used since the transfer line is not long enough to touch the bottom of a 100 liter liquid helium tank. The transfer line has two sides; one has a needle valve while the other end is open. The one with the needle valve goes to the liquid helium tank while the other one goes to the cryostat. If the needle valve on the transfer line is totally open, three holes will be open at the end. Before inserting the transfer line into the liquid helium tank, the needle valve is turned on about 6 turns, which opens half of a hole at the end; then insert the transfer line into the liquid helium tank to about 20 cm above the liquid helium level in the tank. The other end goes to the cryostat. The level of the liquid helium should be determined beforehand. When doing the liquid helium transfer, the valves on the liquid helium tank

should remain off in order to maintain the pressure inside. The transfer line will lower 5 cm every 15 minutes while the pressure in the tank should be monitored at the same time. When the pressure in the tank reaches 1.5~3 psi, the transfer line should not be lowered any more. After about 15~20 minutes, the temperature starts to goes down. Set the desire temperature on the Lake Shore 330. For the PID, at temperature above 20 K, set P=200, I=114, D=100. At the temperature below 20 K, set P=20, I=20 while D is kept the same. The heater is set to the medium range. When the temperature reaches the desired temperature, the needle valve on the transfer line should be almost turned off, with only 1/8 circle open. It takes some time for the temperature to be stable. If the cooling power is too big, for example, when the heater already reaches 100% but the temperature is still dropping, the needle valve needs to be turned down a little bit. It is good to keep the heater range on Lake Shore 330 to be 40~60%.

II-4 Conclusion

In this chapter, graphene device fabrication, measurement equipment, and measurement circuit setup have been discussed. These are very important steps because a good device and measurement system are the prerequisite of the good data. They make it possible to learn the physics in graphene.

Chapter III
Manipulation of Graphene Mobility and Charge Neutral Point Using Molecules

III-1 Introduction

Graphene have many prominent properties, and the large carrier mobility is believed to be most excellent one, which makes graphene an attractive candidate for future electronic device applications [Geim, *et al.* 2007]. The underlying mechanism behind the graphene carrier mobility has been a subject of extensive investigations ever since the inception of graphene devices [Novoselov, *et al*. 2004, Hwang, *et al*. 2007, Morozov, *et al*. 2008, Chen, *et al*. 2008]. In SiO_2/Si-supported graphene devices, the mobility typically varies from 2000 to 20000 $cm^2 V^{-1} s^{-1}$ [Tan, *et al.* 2007]. By removing SiO_2, much higher mobility (2×10^5 $cm^2V^{-1}s^{-1}$) has been obtained in the suspending graphene devices, suggesting the importance of the Coulomb scattering in graphene transport[Du, *et al.* 2008, Bolotin, *et al.* 2008]. Although such elaborate device fabrication is clearly effective, the mobility of finished devices is fixed thereafter and can vary from device to device. In addition, suspending graphene device is by no means easy to fabricate and it is very fragile, which make it impossible for large-area application.

Graphene is also known to be sensitive to molecular adsorption or photoresist residues [Schedin, *et al.*, 2008, Casiraghi, *et al.* 2007]. They are believed to be the sources of long-range scattering which limits the carrier mobility. People have tried different kinds of annealing, such as vacuum annealing, current annealing and annealing in the foaming (forming?) gas [Moster, *et al.*, 2007], to remove these residues to improve graphene mobility. In our work, however, by decorating the SiO_2 -supported graphene device with certain kinds of molecules as a charge reservoir, we first demonstrate a significant enhancement in graphene carrier mobility. By transferring charges between graphene and the molecule reservoir, we show a remarkable reversible tunability in mobility (4000-19000 $cm^2V^{-1}s^{-1}$) in the same device, which unambiguously proves that the charged impurity scattering is the prevailing mechanism for graphene mobility. In addition, the charge neutral point or the Dirac point can also be independently tuned over a wide gate voltage range. The reversible tuning is useful for fabricating large-area graphene devices such as nonvolatile memory with enhanced sensitivity.

In this chapter, first of all, the effects caused by the toluene molecules in the graphene device are shown. Most of the data are from one representative device. Then a model that explains those effects are discussed. Finally, it is the conclusion.

III-2 Using Toluene Molecules on Graphene

The single-layer graphene devices are fabricated using the method described in Chapter II. They are all either in the four-terminal or the van der Pauw geometry to eliminate the contact resistance. For the purpose of compare, a set of measurement has been done on pristine samples before placing the toluene molecules. The mobility of all pristine single-layer graphene devices ranges from 1,500 to 5,500 $cm^2V^{-1}s^{-1}$ at room temperature.

To control the charge environment, we place a layer of toluene molecules on top of the as-fabricated graphene devices. The toluene used here is in High Performance Liquid Chromatography (HPLC) grade. When adding the toluene molecules, the sample keeps connecting to the sample holder of the continuous flow cryostat system with all the pins grounded. The toluene is added drop by drop. The next drop would be added when there is no visible liquid toluene left on the substrate from the previous drop. Eventually, the toluene will evaporate away from the sample, but it will not be completely dried. There will be a layer of toluene residue left on top of the sample even after it has stayed in the vacuum for as long as a month. The thickness of the residue layer can vary from sample

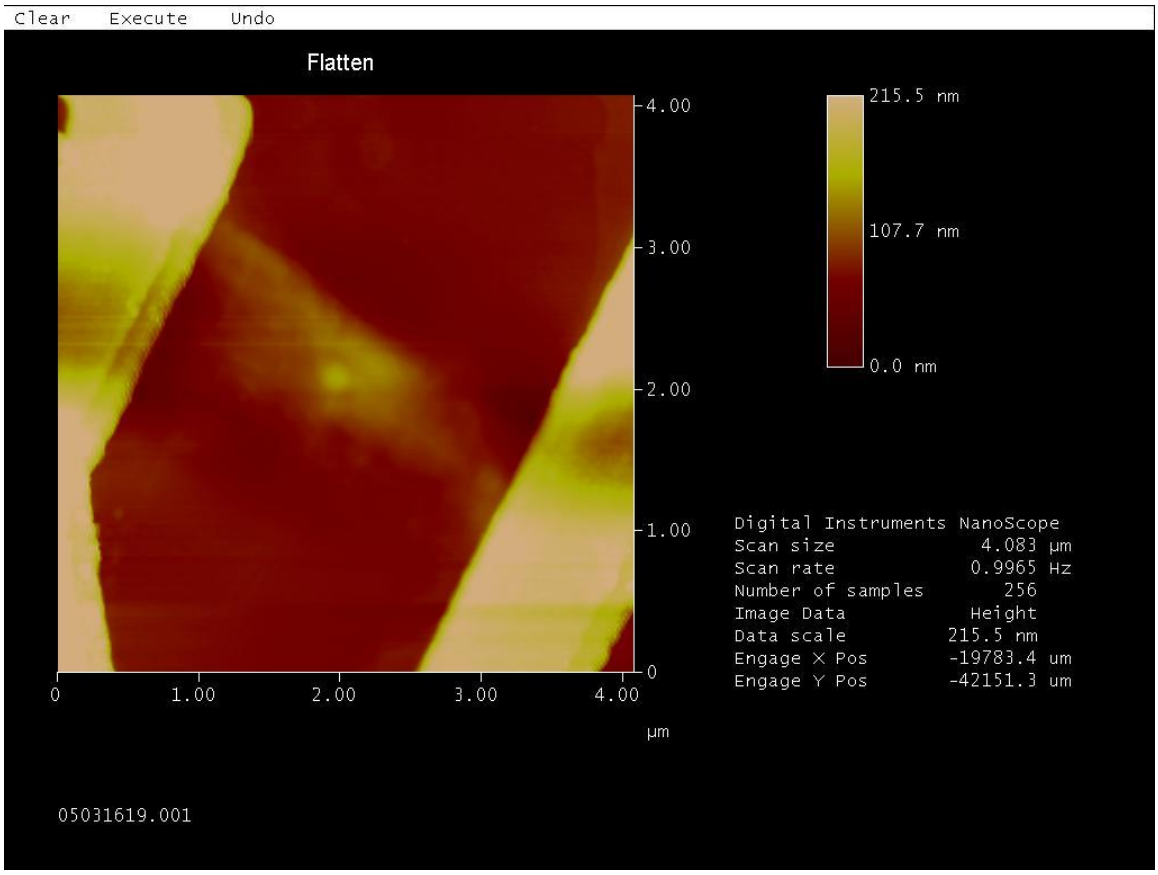

Figure III-1 An AFM image of a graphene device with toluene molecules on top. The thickness of the toluene molecule layer is about 100 nm

to sample even the same amount of toluene is applied. But for the same device, the more toluene is added; the thicker residue layer is obtained. Figure III-1 displays an AFM image of a graphene device after 4 drops toluene. The remaining toluene residue layer on top has a thickness of about 100 nm.

III-3 Memory Effect and Resistance Relaxation Effect

The measurement is performed after the sample was dried in vacuum overnight. Graphene resistivity vs. gate voltage V_g of a pristine graphene device (i.e. without molecules) is shown by the blue curve in Figure III-3. The carrier mobility is 5,500 $cm^2V^{-1}s^{-1}$ and the Dirac point is located at +25 V at room temperature. After two drops of toluene are applied, which is shown as the red curve in Figure III-3, the device shows similar behavior as the pristine sample except the Dirac point is shifted by a few volts towards the negative V_g, and its mobility is increased slightly, from 5,500 to 6,100 $cm^2V^{-1}s^{-1}$. This behavior indicates that the toluene molecules density on graphene is not sufficiently high to play any significant role in graphene transport. We put two more drops of toluene solution on the same device. Now as V_g is swept, two resistance peaks appear (blue curve in Figure III-4). We repeat gate sweeps with various starting and finishing V_g and with different voltage ranges. The hysteresis loop starts to appear if

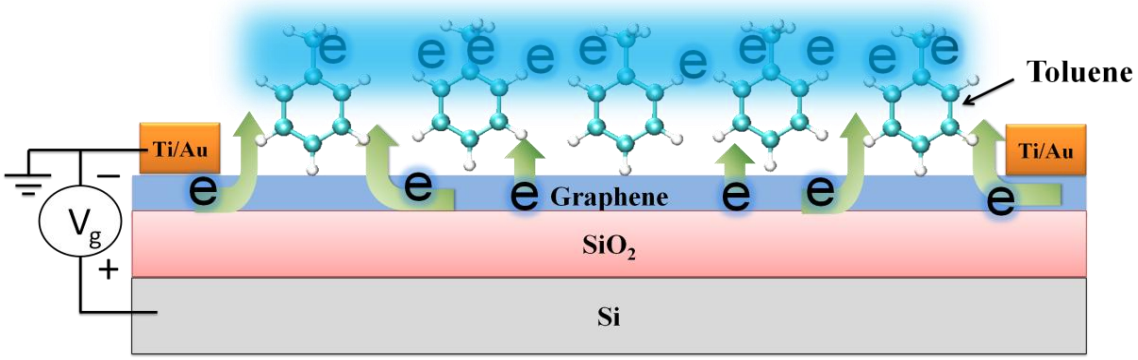

Figure III-2 A cartoon of graphene device dressed with toluene molecules

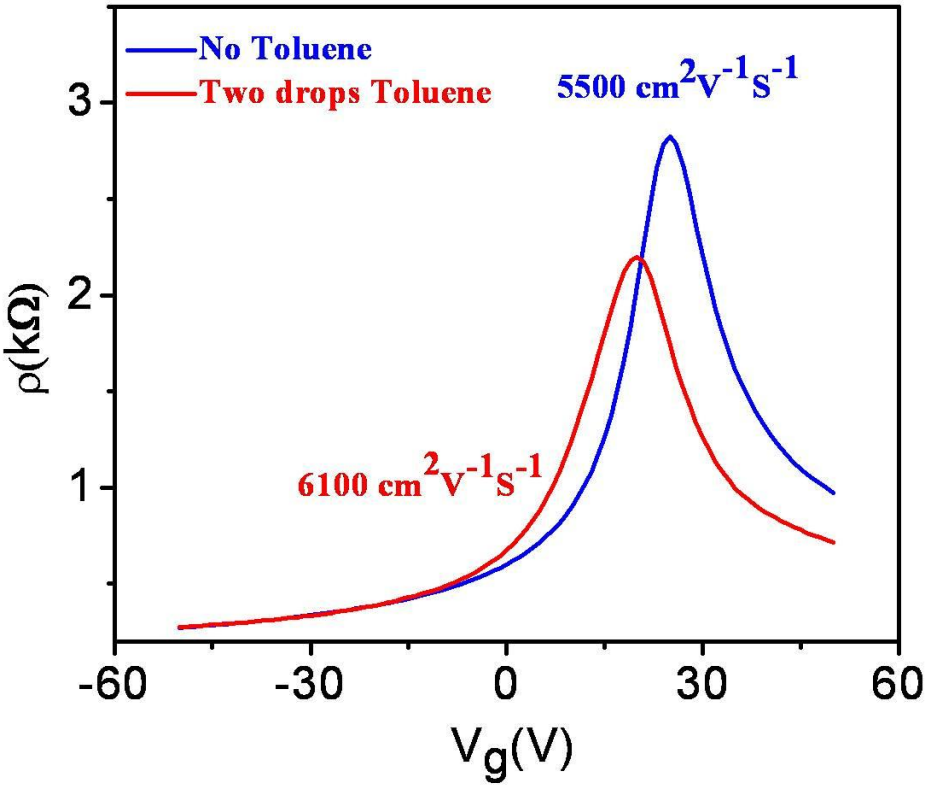

Figure III-3 Resistivity vs. gate voltage for pristine graphene (blue) and the same device receiving two drops of toluene solution (red).

V_g exceeds a certain value in the previous sweep. We find that the peak position depends sensitively on the maximum voltage in the previous sweep. More details about this will be discussed in the next Chapter. This phenomenon suggests a familiar bi-stability, i.e. two possible resistance states for a given V_g. In other words, the carrier density in graphene thus the resistivity is not unique to V_g. We know that such bi-stability does not exist in the pristine graphene; therefore, the bi-stability must be caused by molecules. It should be pointed out that the addition of molecules on graphene does not provide a parallel current path, for the molecules are much more resistive than the graphene channel even if they are in high densities.

Another surprising consequence is the carrier mobility enhancement in graphene. After 4 drops of toluene solution are applied, the room temperature mobility increases to 9,500 $cm^2V^{-1}s^{-1}$. Like what has been discussed above, graphene mobility is known to be sensitive to organic molecules such as photoresist residues [Schedin, *et al.*, 2008, Casiraghi, *et al.* 2007]. They can trap charges and consequently cause additional scattering which degrades the graphene mobility. Apparently, toluene molecules do not adversely affect the carrier mobility; on the contrary, they enhance the mobility by a factor of 170%, which is entirely unexpected.

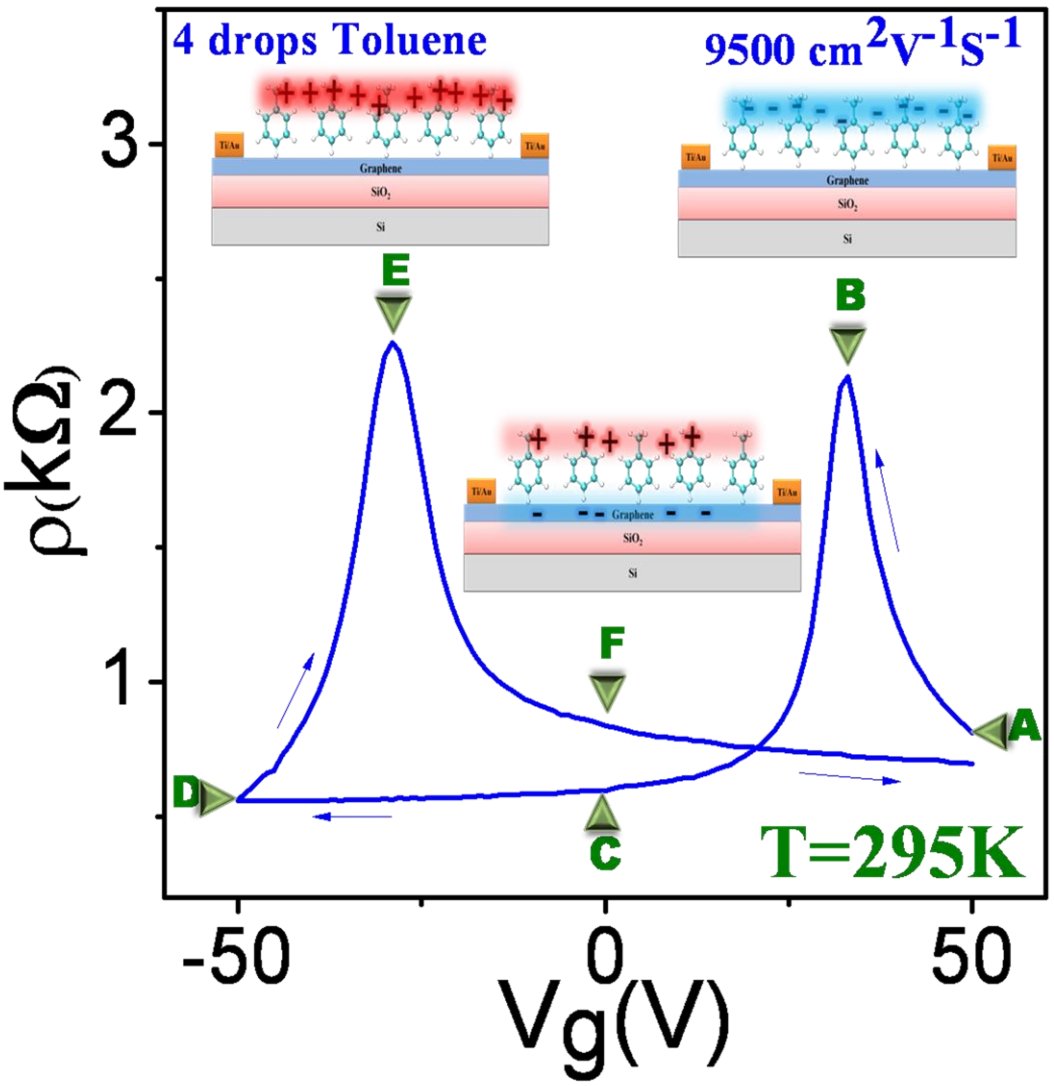

Figure III-4 Resistivity vs. V_g for the same device with four drops of toluene solution. Points A through F represent different states of graphene plus toluene molecules as described in the text. The three cartoons represent different charge states at B, E and F.

At room temperature, we found another slow irreversible resistivity relaxation process. Upon the application of a fixed V_g, the graphene resistance undergoes a continuous change as a function of time, which is shown in Figure III-5, indicating a slow carrier density change in graphene. Surprisingly, no matter whether the set voltage is positive or negative, i.e. graphene initially charged with electrons or holes, the graphene resistance overall always climbs up or moves towards the charge neutral point, suggesting that graphene does not prefer to carry electrons or holes. The presence of molecules nearby provides a reservoir that accepts and stores the charges. The characteristic time for the relaxation process is about 2,000s for this device at room temperature, which is much slower than gate sweeping; therefore, this time-dependent process is not visible in normal gate sweeps.

III-4 Tunable Graphene Mobility and Charge Neutral Point

In the toluene-dressed graphene devices, we found that the field effect mobility of graphene can be widely tuned. We first set V_g at an arbitrary value, wait for a certain amount of time, and then quickly cool the device to low temperatures (~15 K / minutes) while the same V_g is always kept. At 20 K, the double peaks and associated hysteresis disappear, in the meantime, the time dependence in resistance is no longer present.

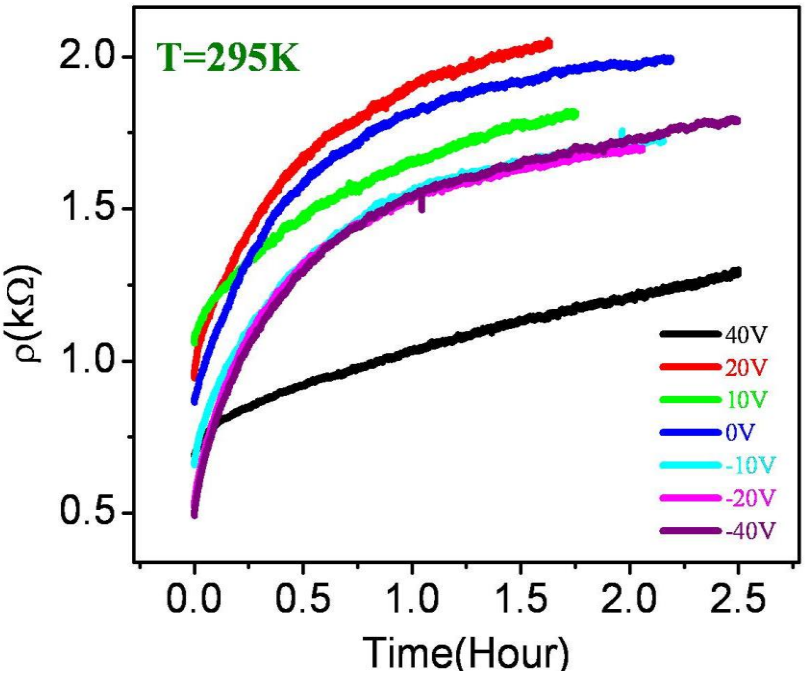

Figure III-5 Resistivity of graphene as a function of wait time for various set gate voltages (0, ±10, ±20, and ±40 V) at room temperature. Graphene was at different gate voltages from the set voltages. After a new set voltage is applied, the resistivity always increases and approaches 2.2 kΩ, the charge neutral point.

Resistivity before cooling down (Ω)	Mobility ($cm^2 V^{-1} S^{-1}$)
1892	19200
1730	15300
1378	13100
892	9500
757	7700
540	4600

Table III-1 Relationship between room temperature resistivity and low temperature carrier mobility.

Varying V_g only modulates the carrier density in graphene, just as in regular pristine graphene. At 20 K, we find that the graphene mobility is generally enhanced (Figure III-6). Depending on the resistivity value in the pre-cooled state which can be set by controlling the wait time in the resistivity relaxation process, the resulting low-temperature mobility can vary literally anywhere from 4,600 to 19,200 $cm^2V^{-1}s^{-1}$, varying by a factor of 4.2. Note that the lower limit is even lower than that in the pristine state, i.e. 5,500 $cm^2V^{-1}s^{-1}$. Table III-1 shows the one-to-one relationship between the room-temperature initial resistivity and the final low-temperature mobility. The key to turn the carrier mobility is the pre-cooled charge state which can be accurately monitored and set by the time-varying resistivity. Clearly, the closer the graphene is to the charge neutral state (i.e. resistivity maximum) at room temperature, the greater the low-temperature mobility becomes.

Not only the carrier mobility can be widely tuned, the position of the Dirac point can be independently tuned as well. Figure III-7 shows that low-temperature mobility can be kept relatively high, while the Dirac point can be set at different positions. This is in stark contrast to earlier observations that the Dirac point shift is correlated with the mobility [Tan, *et al.*, 2007, Chen, *et al.* 2008]. High mobility in all cases is obtained by setting the device at an arbitrary gate voltage at high temperature, waiting the resistivity of graphene

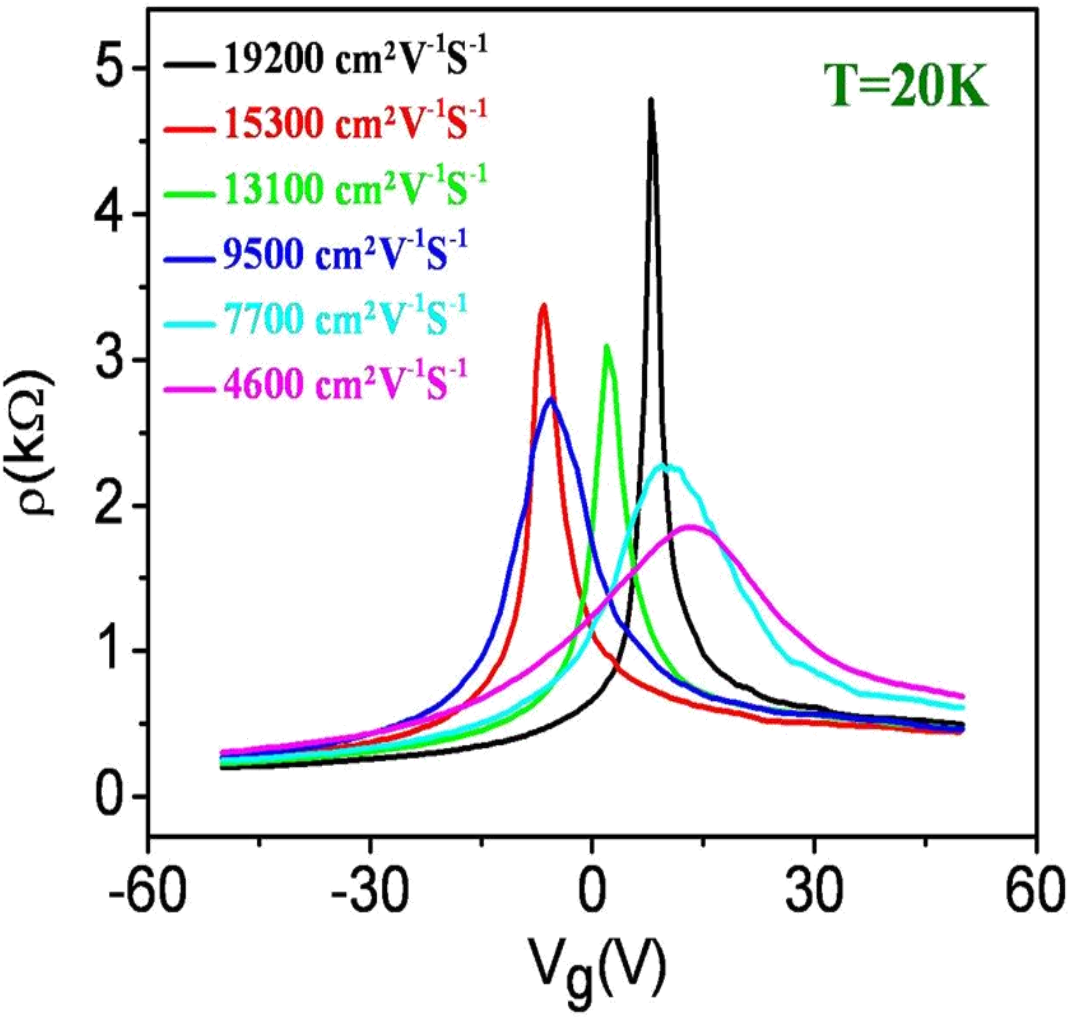

Figure III-6 Resistivity vs. V_g of a graphene device cooled to 20 K from room temperature with different initial resistivity values. Carrier mobility is shown for different cooling conditions.

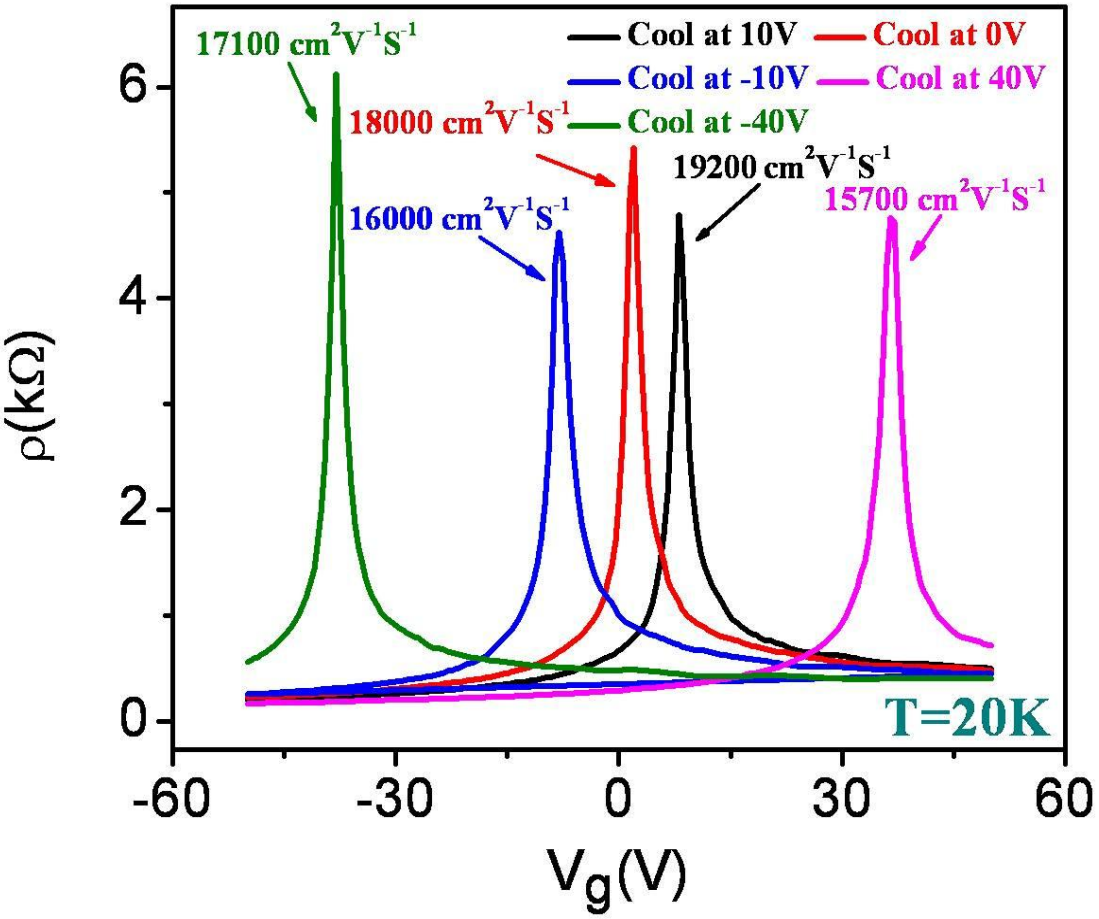

Figure III-7 High mobility but widely different Dirac point positions are obtained with different set voltages and long wait times.

to climb up to or very close to the charge neutral point, and cooling the device quickly to 20 K. The final low-temperature Dirac point position is settled at or close to the set gate voltage at high temperature.

III-5 Model and Discussion

III-5-1 Charge Transfer Model

From above, we know that this seeming dirty toluene residue molecules layer actually cause positive effects (memory effect, increased mobility, tunable mobility and charge neutral point) on the graphene device. To understand this, a charge-transfer model needs to be applied. In this system, graphene sheet and the toluene molecules can be considered as one capacitor plate, and the Si back gate as the other. Both toluene molecules and graphene can be charged up by gate voltage (Figure III-2), but between them there is an energy barrier. The height and width of this energy barrier depends on how well the molecules bond to graphene surface. Molecules can only get charge from graphene through the energy barrier. This can be viewed as a potential barrier separating two wells, similar to the Fowler-Nordheim tunneling in semiconductor devices. The charge can transferred back and forth between graphene and molecules by controlling the

electrical field provided from back gate voltage. The amount of charges transferred can depends on the strength of the electric field.

III-5-2 Explanation for Memory and Relaxation effect

When a sufficiently large positive V_g is applied (point A on blue curve in Figure III-4), the graphene sheet is negatively charged almost instantly. In the meantime, the wells are tilted in one way and the molecules are also negatively charged. As V_g is decreased, the charges on graphene are first decreased and then completely depleted at B (V_g ~ +33 V), where the charge neutral point or the Dirac point is attained, as indicated by the resistance maximum. From the capacitance of the device C_g (~ 115 aF/m^2) and the position of the charge neutral point (V_g^B), we can readily estimate the amount of charges on toluene molecules, i.e. $q_B = C_g \cdot V_g^B = 2.4 \times 10^{12}$ electrons/cm^2. As V_g is ramped down, graphene is gradually loaded with positive charges, as shown by the decrease in resistivity. At V_g =0 (C), the trapped negative charges on toluene molecules, equal or less than q_B, induce the equal amount of positive charges on graphene. As negative V_g is applied, more positive charges on graphene are accumulated and the resistivity decreases continuously. Meanwhile, the negative charges on toluene molecules are decreased and depleted, and then positive charges are gradually loaded onto molecules.

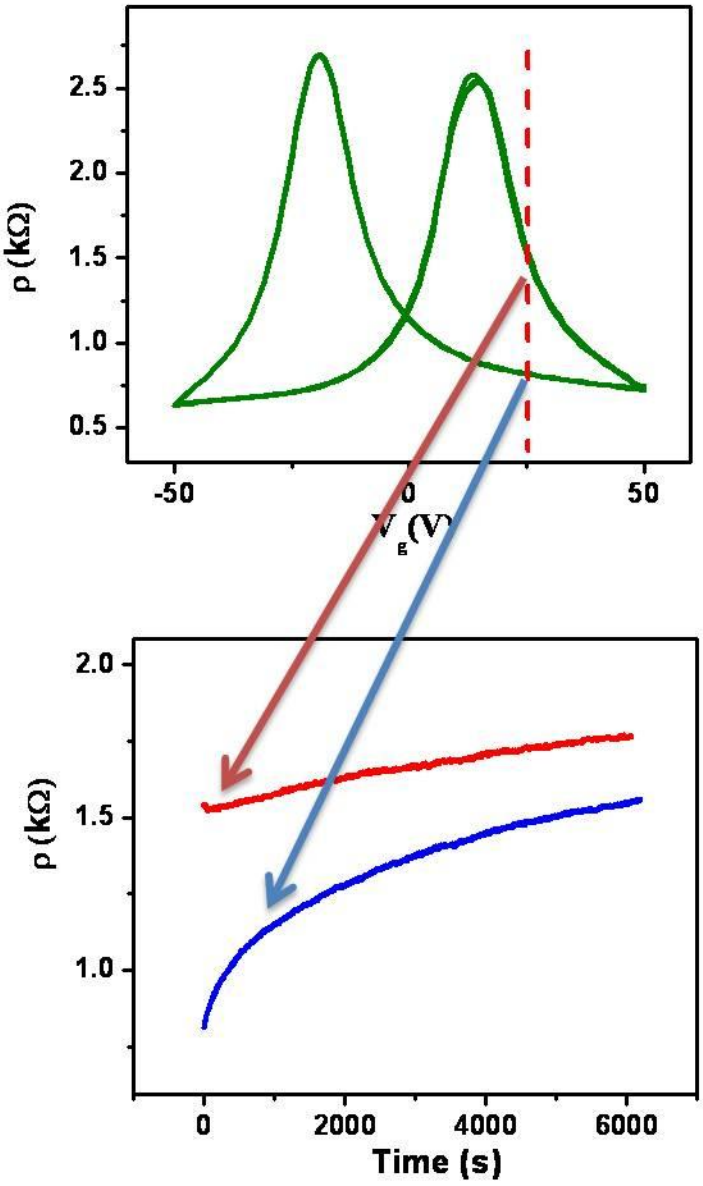

Figure III-8 The relaxation behavior at the same gate voltage (+25V) but different charge state.

At point D, the toluene molecules are replenished with positive charges. When V_g is swept back towards zero, similar processes occur. Another charge neutral point is reached at E. At V_g=0, graphene is negatively charged (F) and then more negatively charged at higher positive V_g. In the meantime, the toluene molecules are also replenished with negative charges again, which completes a cycle. Note that there is a small asymmetry between positive and negative side. So, clearly the external electric field alters the charge state in molecules which is not a unique function of the electric field, and in turn results in the hysteresis in graphene resistivity.

The sign and amount of charge between graphene and molecules can be tuned back and forth by varied gate voltage. However, at any fixed gate voltage, overall it seems to be mono-directional, i. e. always from graphene to molecules, no matter the charge is positive or negative. The reason is rooted in the nature of graphene. Graphene has very unique band structure in which the electron density-of-state varnishes at the Dirac Point. So graphene always prefer to stay charge neutral. When it is bonded by some charge reservoir which can store the charge, such as the toluene molecules, graphene will discharge the excessive charge to this charge reservoir. How much charge can be discharged from graphene depends on the external electric field, the discharge ability of graphene and the charge acceptance ability of the charge reservoir. Toluene is not the only

molecule can accept the charge from graphene. More details are discussed in next chapter. The characteristic times strongly depends on the charge state on the molecules and graphene. If the charges on the graphene and molecules have different sign, the characteristic time is short while if the charges on the graphene and molecules have some sign, the characteristic time is long. In Figure III-5, the data is measured as following: First set the V_g to 50 V, then ramp it to the selected value. From Figure 4, we know that the charge sign on graphene and molecules at +40 V is different from other gate voltages (Dirac point at 36 V). At +40 V, the charge sign on both graphene and molecules are negative while at other gate voltages in Figure III-5, the charge sign are different. And we can see that the characteristic time at + 40 V is larger than other gate voltages. In Figure III-8 (b), the two curves are measured at the same V_g (+25V), but with different charge state and they have different characteristic time too.

III-5-3 Explanation for Tunable Graphene Mobility and Charge Neutral Point

At low temperature, there are no memory and relaxation effects. This means that the initial charge state on molecules is frozen. The varying gate voltage only modulates the carrier density on graphene. It occurs because as temperature decreases, the potential barrier at the interface of graphene and molecules becomes larger and larger,

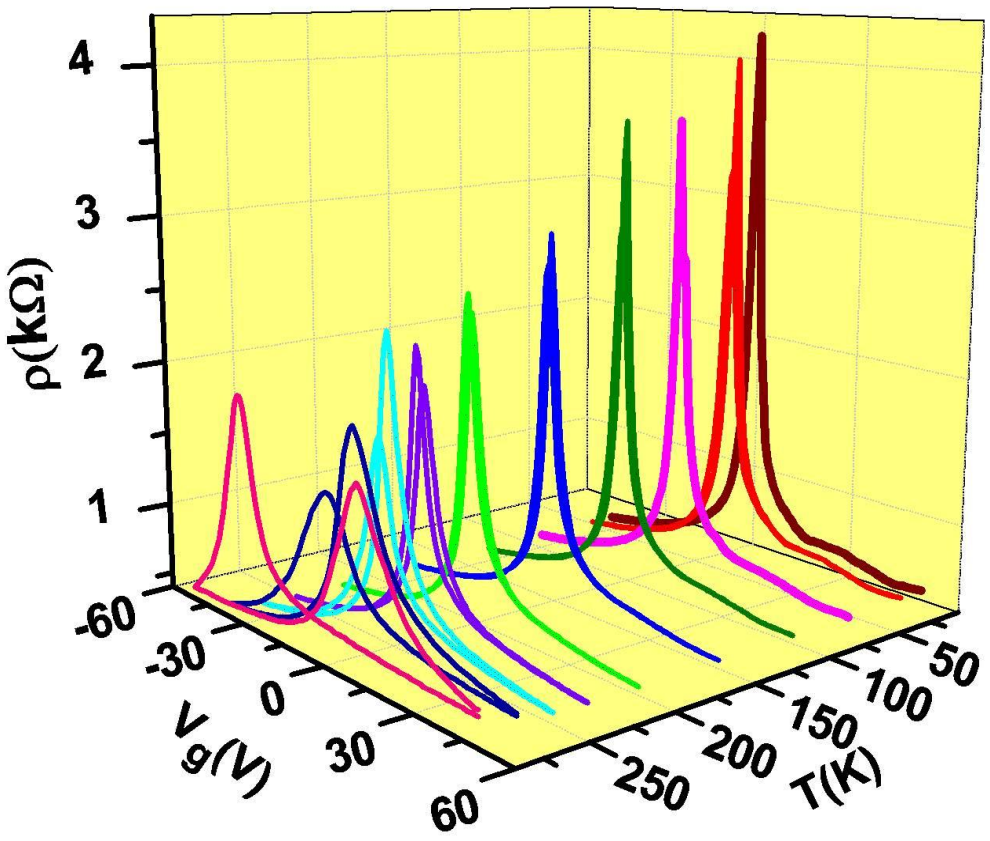

Figure III-9 Gate voltage sweeps at different temperatures during warming starting from 4 K.

and then charge transferring become more and more difficult. Figure III-10 displays ρ vs V_g at different temperatures. When the temperature is below 200 K, there is no obvious noticeable hysteresis behavior in the curves. So when the mobility is tuned, in low mobility cases, charges in the pre-cooled state are so bountiful that most of them can be trapped during cooling. At low temperature (20 K), they have nowhere to go but stay on graphene and cause a lot of scattering to the carriers. In high mobility cases, most charges can be transferred to molecules if the wait time is sufficiently long. At low temperature, when the excess charges are already transferred to molecules, graphene is relatively clean, so we have less scattering. What is more interesting is that in pristine graphene high mobility cannot be obtained just by maintaining the charge neutral state during cooling, which implies that the molecules do more than absorb excess charges on graphene. Here what has been done is nothing but the change of the charge state on and near the graphene sheet. The charge absorbing molecule layer simply provides us a knob to conveniently manipulate the charge environment. These results support that the charged impurities stuck to graphene are the main limiting factor to graphene mobility.

To tune charge neutral point, we first wait the graphene resistivity climbing up to maximum at a fixed gate voltage, for example +40 V. The amount of charge on the molecules is very closed to what the back gate can provide, i. e. C_g *(+40 V). During

cooling, almost all charges stored on molecules at high temperature are retained. At low temperature, these charges produce the same electric field as what a +40 V gate voltage can do on graphene. So we got the graphene Dirac Point at +40 V. The charge on the molecules should distribute very uniformly on top since they don't cause more scattering to the graphene (high mobility is attained here). What they do is providing an electric field screening background to the graphene, just like a floating gate. In some originally low mobility devices (~ 2,000 $cm^2V^{-1}s^{-1}$), after adding molecules, the graphene charge neutral state cannot be reached for similar amount of waiting time. As a result, the low-temperature Dirac point is settled at smaller voltages than the high-temperature set gate voltage, although the mobility is still significantly enhanced (~ 12,000 $cm^2V^{-1}s^{-1}$). This is probably caused by the charged impurities beneath graphene that are largely unaffected by the presence of molecules.

III-5-4 Graphene Mobility Temperature Dependence

As the temperature is raised from low temperature, the mobility stays virtually unchanged blow 200 K (Figure III-9). The hysteretic behavior reappears above ~ 230 K, as the potential barrier at the interface become smaller at high temperatures, which switches on the charging path between graphene and toluene molecules. Note that

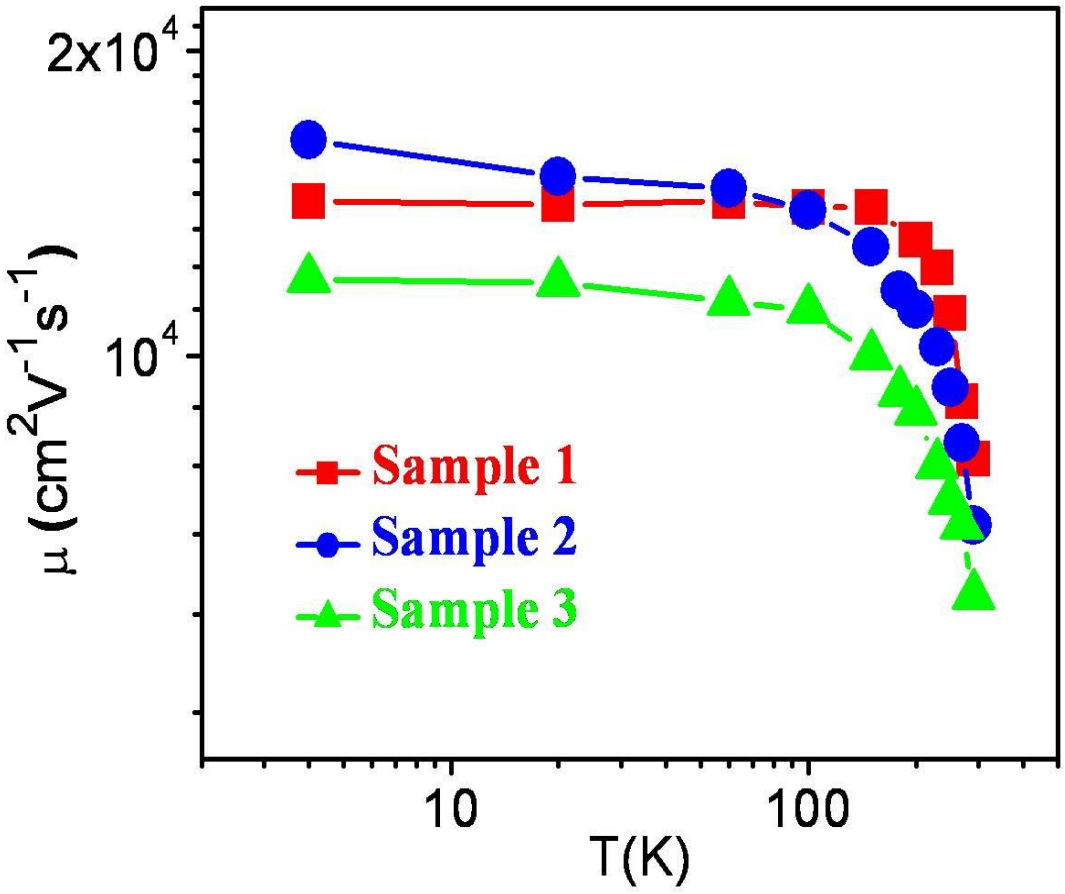

Figure III-10 Temperature dependence of mobility for three devices. The red curve represents data shown in Figure III-9

the mobility remains relatively temperature independent below 200 K and a steep mobility drop (from 13,000 to 7,900 $cm^2V^{-1}s^{-1}$) occurs between 200 and 290 K. Figure III-10 displays the temperature dependence of three devices. The overall temperature dependence is qualitatively similar. The high temperature drop in mobility seems to be consistent with the remote interfacial phonon scattering mechanism [Chen, *et al.* 2008, Fratini, *et al.* 2008].

III-6 Conclusion

In this chapter, we show that a very large tunability in both carrier mobility and the Dirac point can been achieved in the same devices using molecules as a charge reservoir. These seemingly messy organic molecules actually create a rather clean environment for carriers in graphene. Even greater mobility improvement can be expected by exploring different molecules, which may open up new possibilities for investigating interesting physical phenomena at low carrier densities and for fabricating high-speed electronic devices without resorting to removing the substrates.

Reference:

Geim, A. K., *et al*., Nature Mater. 2007, 6, 183–191.

Novoselov, K. S., *et al*., Science 2004, 306, 666–669.

Hwang, E. H., *et al*., Phys. Rev. Lett. 2007, 98, 186806.

Morozov, S. V., *et al*., Phys. Rev. Lett. 2008, 100, 016602.

Chen, J. H., *et al.,* Nature Nanotechnol. 2008, 3, 206 - 209.

Chen, J. H., *et al*., Nature Phys. 2008, 4, 377-381.

Tan, Y. W., *et al.,* Phys. Rev. Lett. 2007, 99, 246803.

Du, X., *et al.,* Nature Nanotechnol. 2008, 3, 491–495.

Bolotin, K., I., *et al.,* Phys. Rev. Lett. 2008, 101, 096802.

Schedin, F., *et al.*, Nature Mater. 2007, 6, 652-655.

Casiraghi, C., *et al.*, Appl. Phys. Lett. 2007, 91, 233108.

Moster, J., et al., Appl. Phys. Lett. 2007, 91, 163513.

Fratini, S., *et al.* Phys. Rev. B 2008, 77, 195415.

Chapter IV
Large Memory Effect in Graphene Based Devices

IV-1 Introduction

The discovery of the atomic layer graphene in 2004 has open up a new direction for materials science. Unlike the conventional 2D system buried at the interface of semiconductors, graphene is open to any physical or chemical modification. Tremendous effort has been put into developing new electronic devices based on this great material, due to its outstanding properties. However, graphene is known as a zero band gap semiconductor, so it seems impossible to turn off a graphene based electronic device. Although some physicists already successfully open a band gap in graphene [Zhang, *et al.* 2007, Han, *et al.* 2007, Wang, *et al.* 2008], the mobility of graphene, which is believed to be the most excellent properties of graphene, is largely decreased at the same time. In Chapter III, we showed a large memory effect graphene devices decorated with molecules on top. The bi-states shown in graphene resistance might be potentially important for developing graphene based memory devices that do not require a band gap. In this chapter, more details about the memory effect and the graphene memory device will be discussed.

IV-2 Large Memory Effect in Graphene

The graphene device fabrication and the method of adding molecules are the same as Chapter III. Red curve in Figure IV-1 is the resistivity ρ vs. gate voltage V_g at room temperature for a pristine sample (not the sample used in Chapter III). The mobility is 3000 $cm^2V^{-1}s^{-1}$ and the charge neutral point V_d is around +25 V. Notice that there is a small hysteresis loop as the gate voltage scans forward and backward. The difference between these two peaks ΔV is 2 V. As we know, Graphene is very sensitive to adjacent environment due to its unique electronic band structure and two dimensional nature. This small loop is believed to originate from the charge trapping and detrapping from the neighboring absorbents such as water molecules [Wang, *et al.*, 2010, Liao, *et al.* 2010]. In our work, by intentionally adding molecules, we provide more charge trapping sites and the effect is amplified. After four drops of toluene solution, before any gate sweeping, at V_g = 0 V, the resistivity of the graphene was already very closed to the charge neutral point resistivity in pristine sample, meaning that at this point, the Dirac point of the graphene with toluene molecules was already closed to 0 V. Then now as we sweep gate voltage in the same range (from -50 V to +50 V) and sweeping rate (0.2 V/s) as we did on the pristine graphene device, a much larger hysteresis behavior is found, which is shown as the blue curve in Figure IV-1. There are two resistivity peaks, one is at +14 V and

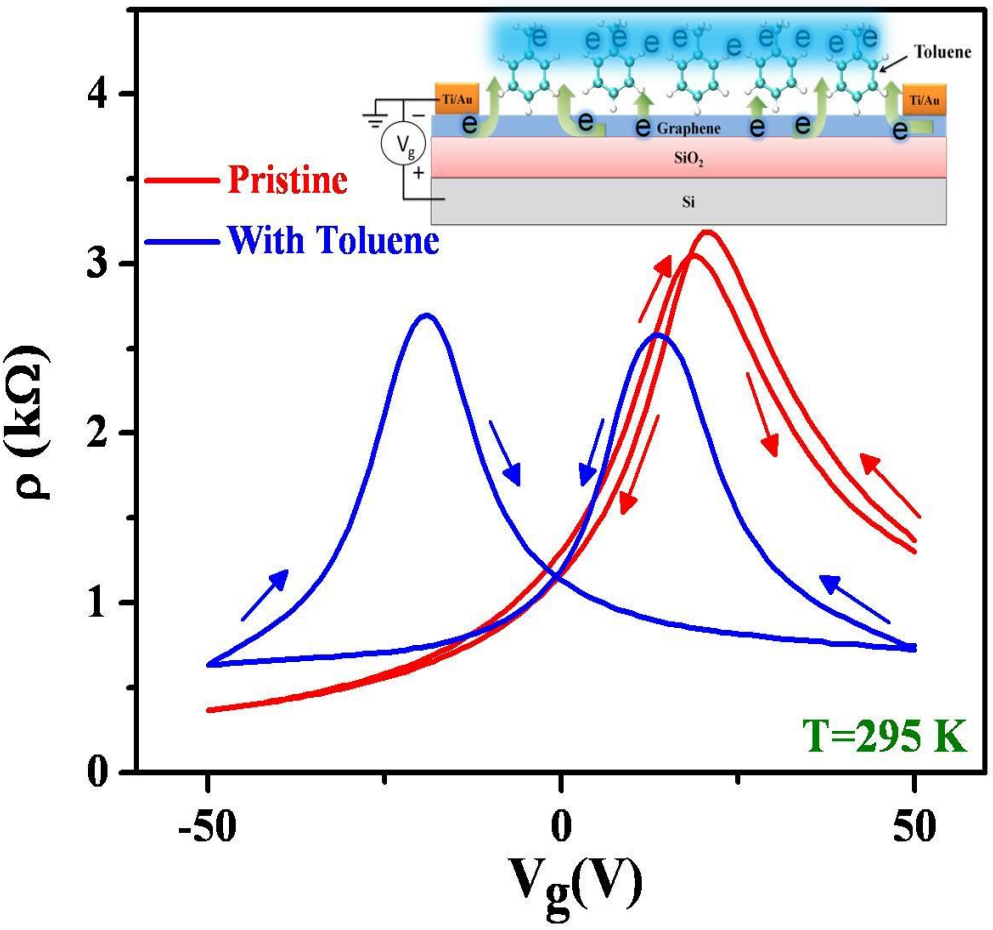

Figure IV-1 Resistivity vs gate voltage for a sample before (red) and after (blue) adding the toluene molecules. Inset shows a cartoon of graphene device dressed with toluene molecules

the other is at -19 V. The difference between these two peak positions ΔV is 33 V, which is much larger than the pristine graphene sample (2 V). Notice that the peak resistance is a little bit smaller than that of the pristine sample.

The memory effect depends sensitively on the gate sweeping rates. Figure IV-2 shows ρ vs. V_g at three different gate sweeping rates. The slower rate to sweep the gate, the larger hysteresis loop is found. For example, for the fastest sweeping rate (2 V/s), we get ΔV equal to 10 V, while for the slowest sweeping rate (0.02 V/s), ΔV is 47 V. This is because the charge transferring process between graphene and toluene molecules has a certain time scale. At a faster gate sweeping rate, we are getting closer to the pristine graphene. Notice that at a faster rate, the resistance at charge neutral point gets closer to that of the pristine graphene. If the gate sweeping rate is so high that the charge has no chance to be transferred to the toluene molecules, we do not expect to see any hysteresis loop. The memory effect also changes with the gate sweeping range. In Figure IV-3, the gate voltage is swept at a fixed rate but in three different ranges. When sweeping gate from -25 V to +25 V, the memory effect was already largely reduced, ΔV is only 2 V, compared to ΔV=33 V for gate sweeping from – 50 V to +50 V. For a smaller gate range, which is from -15 V to +15 V, no hysteresis loop is found and the only one charge neutral point stays close to 0 V, just like a plain graphene sample.

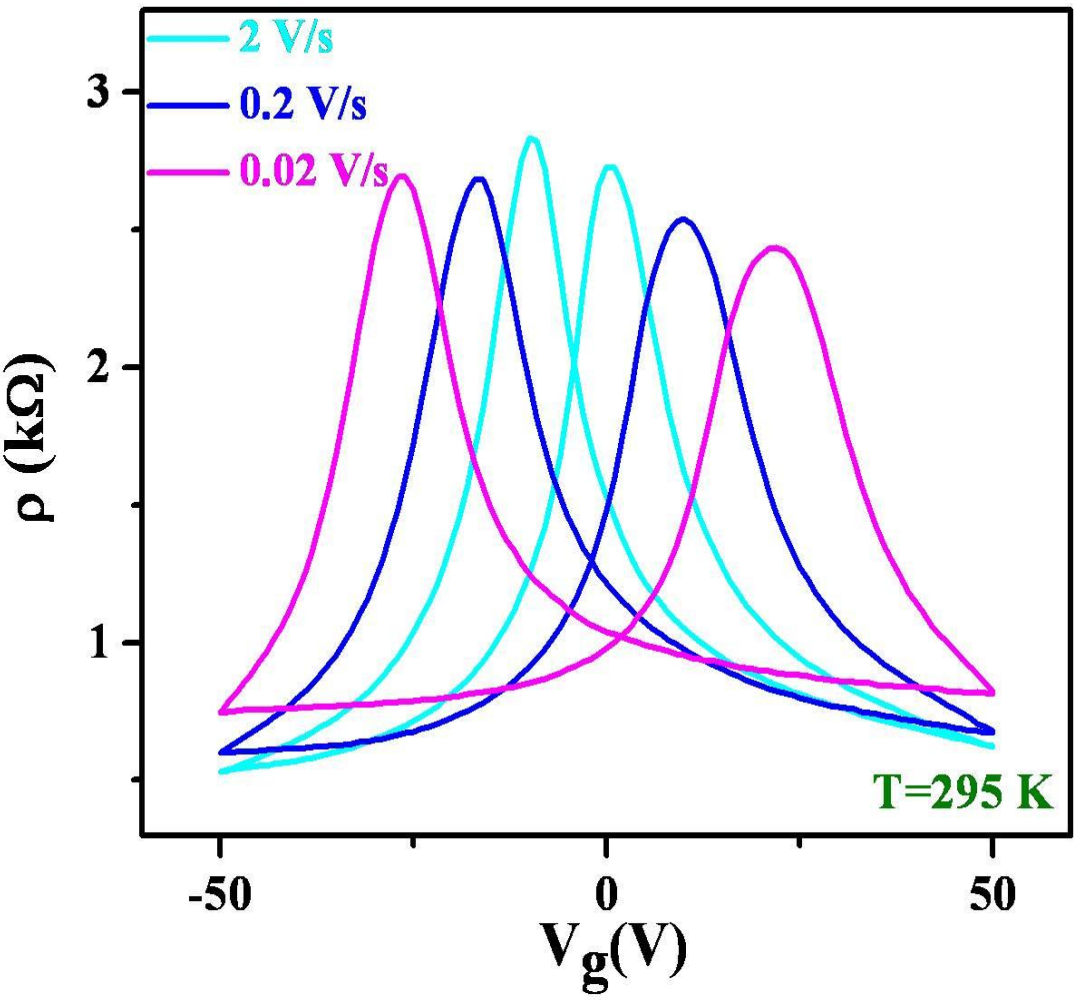

Figure IV-2 Resistivity vs gate voltage from -50 V to +50 V at different gate sweeping rates.

In Chapter III, we have claimed that graphene, toluene molecules, and the energy barrier between them are acting like one potential barrier separating two wells, the amount of charge transferred from one well to the other, namely, from toluene molecules to graphene, depends on the strength of the electric field. When sweeping the gate voltage at a large range, such as from - 50 to +50 V, the two wells can be tiled on both side at a large degree, charge can be transferred between toluene molecules and graphene back and forth. But for a very small range, i. e. from -15 to +15 V, the electronic field is not strong enough to tile the wells, and charge transferring cannot happen at this gate sweeping rate. So graphene behavior is like a normal sample, no memory effect and charge neutral point stays at 0 V. In Chapter III, we know that another knob to control the memory effect is temperature. The inset (a) and (b) in Figure IV-3 show the ρ vs. V_g at three lower temperatures in gate range from -50 to 50 V and gate sweeping rate at 0.2 V/s. At 270 K, ΔV already decreased to 2 V, while at 250 and 20 K, no hysteresis loop behavior was found.

IV-3 Read and Write Operations in a Graphene Memory Device

From the discussion above, graphene and molecules can form a memory device. In this device, toluene molecules are used to store charges, and graphene works

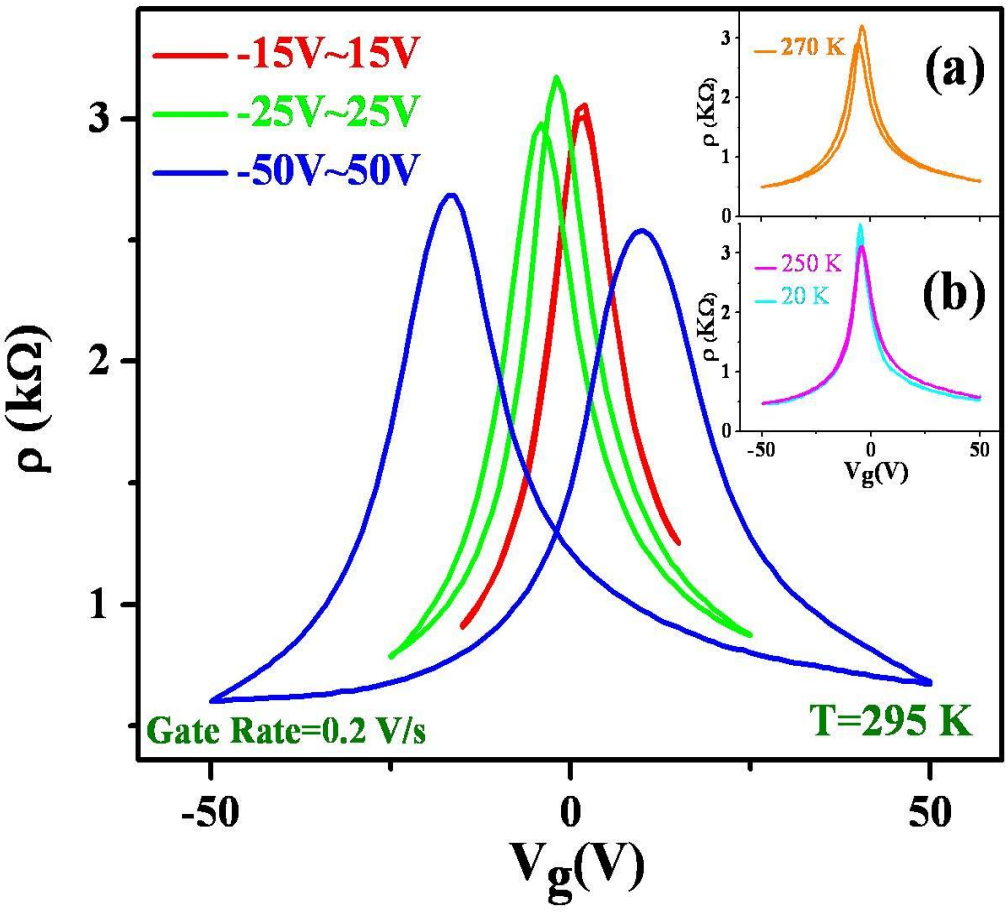

Figure IV-3 Resistivity vs gate voltage from different ranges with gate sweeping rate at 0.2 V/s

as a sensor to detect the charge state on the molecules. Figure IV-4 displays three states of the graphene memory device, which correspond to no charge, positive charge, and negative charge on molecules. If there is no charge on the molecules, the graphene Dirac Point will stay at or close to 0 V which denotes the "0" state (red curve). When there is some positive charge on the molecules, the electric field produced by the positive charge will shift the ρ vs V_g characteristic curve to the left which denotes the"-1" state (blue curve). Similarly, negative charge on the molecules will shift the curve to the right, which denotes the "+1" state (green curve). To read this device, we just need to monitor the graphene resistivity. If only two states are needed, graphene resistivity at V_g =0 V can be recorded. High resistivity corresponds to "0" or "No Charge" state while low resistivity corresponds to "1" or "Charge" state. Depends on the charge on the molecules and the mobility of the graphene, the ratio of these two resistivity could be very high (up to 1000% in high mobility sample). Recall that the mobility of graphene is increased after adding the toluene molecules. If three states are needed, a small bi-direction gate voltage sweeping can be used. For example, V_g can first be swept to +2 V and then to -2 V, while the resistivity of graphene is recorded at the same time. If ρ (+2V) –ρ (-2V) = 0, the device is at "0" state. If ρ (+2V) –ρ (-2V) < 0 or >0, then the device is at "-1" or "+1" state respectively.

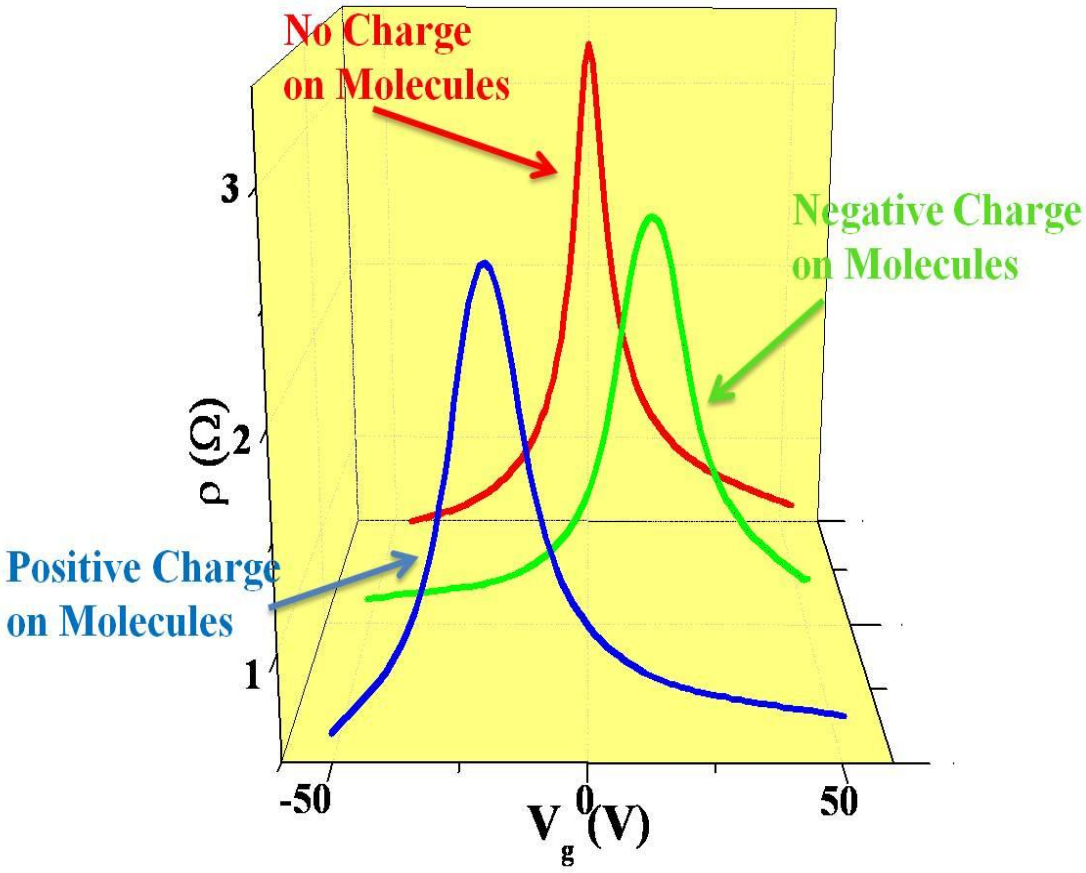

Figure IV-4 If there is no charge on the molecules, graphene will have 0 V Dirac Point (red curve). Negative charge on the molecules shifts ρ vs V_g curve to the right (green curve) while positive charge shifts it to the left (blue curve).

To write the device, which is basically changing the charge state on molecules, we can just apply a large gate voltage. In Figure IV-5, four cycles of gate sweeping processes are applied. All of them are performed in the same rate (0.2 V/s). The gate voltage is swept from the same gate voltage i. e. +30 V, but to a different gate voltage and back. Before each cycle, a large positive gate voltage (+50 V) is applied to upload negative charge to the toluene molecules, which is indicated by the +18 V graphene Dirac Point (the blue open circles in Figure IV-5). In Cycle 1, gate voltage is swept from +30 to +10 V and back. The backward and forward curves almost overlap and starting point and ending point are almost the same, which means that charge on molecules does not change in this cycle. The similar behavior is found in Cycle 2. However, in Cycle 3, when the gate voltage is swept from +30 to -10 V and back, the disparity between the backward and forward curves starts to appear. The ending point does not go back to the starting point. And the Dirac Point moves from +18 to +8 V. This indicates that a certain amount of negative charge on the molecules has been depleted. The remaining less negative charge induces less positive charge on graphene, and as a result we have a smaller Dirac Point gate voltage. The depleted negative charge is $C_g \times (18V\text{-}8V) = 7.2 \times 10^3$ electron/μm^2, where C_g =115 aF/μm^2 is the back gate capacitance. As the gate voltage is swept further, we could write positive charge to the molecules. In Cycle 4, when the gate voltage is swept from 30 to -50 V and back, the new Dirac Point appeared

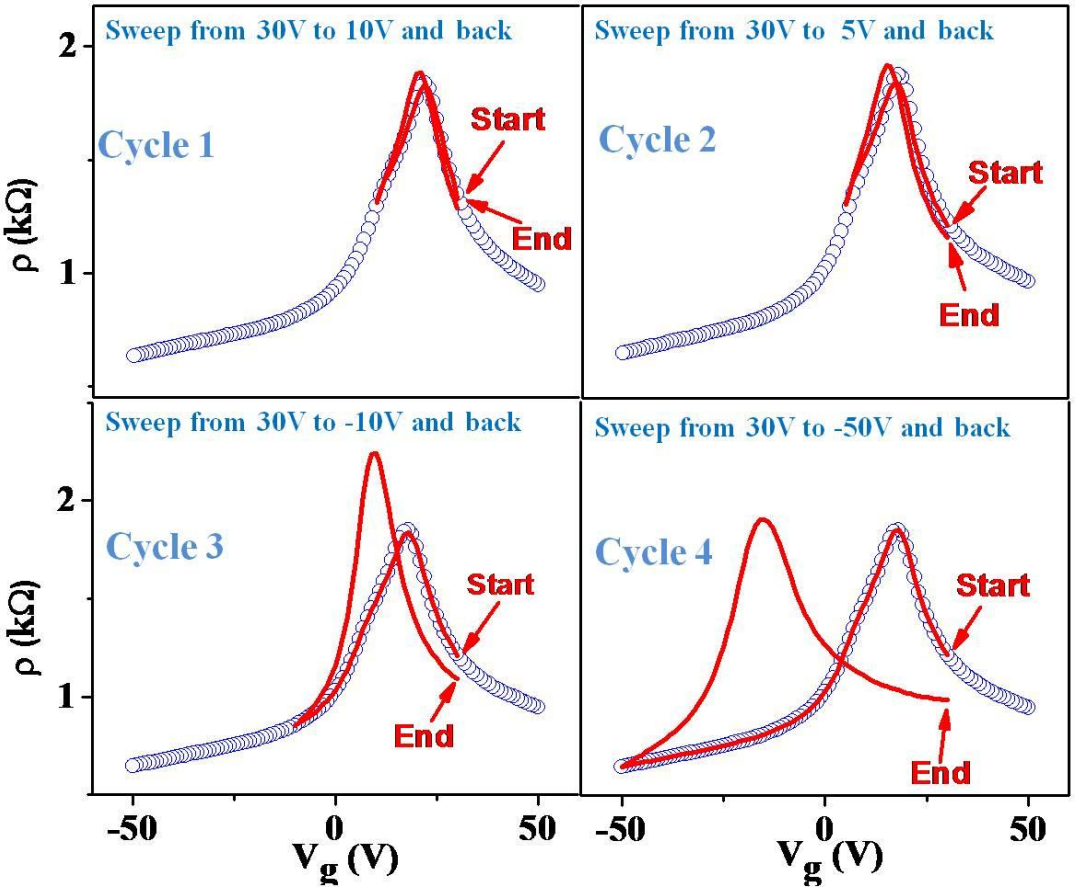

Figure IV-5 Writing process of graphene memory device. Before each cycle, a large positive gate voltage (+50 V) is applied to upload positive charge on molecules (blue open circles). In Cycle 1, 2, 3, and 4, writing gate voltage is first swept from 30 V to 10 V, 5 V, -10 V and -50 V respectively and then back to 30 V.

at -15 V, meaning that the negative charge on the toluene molecules is totally depleted and a large amount of positive charge has been loaded. This finishes a writing process.

IV-4 Possible Reasons for the Memory Effect

Why can toluene result in this large memory effect in graphene? First of all, we have a great amount of toluene molecules on graphene and they are stable even in the vacuum. This provides many trapping sites on top of graphene for the charge. Figure IV-7 (a) shows an optical image of a graphene sample dressed with toluene molecules after staying in the vacuum for a month. After we remove the toluene layer by acetone, the memory effect disappears. We have also tried other different solvents on the graphene samples, such as hexane, chloroform, and ethanol. None of them can leave a visible residue layer on graphene from optical microscope. We find no large memory effect in the samples using those solvents but they do show large memory effect after adding toluene molecules (Figure IV-6). Secondly, the memory effect may be related to the negative electron affinity of toluene. In Figure IV-7, the data are shown based on the samples dressed with three different kinds of molecules: toluene, naphthalene, and anthrancene, whose electron affinities are -1.1 eV, -0.2 eV, and 0.5 eV respectively. All of them can leave a layer of molecules on the graphene. As we added more and more

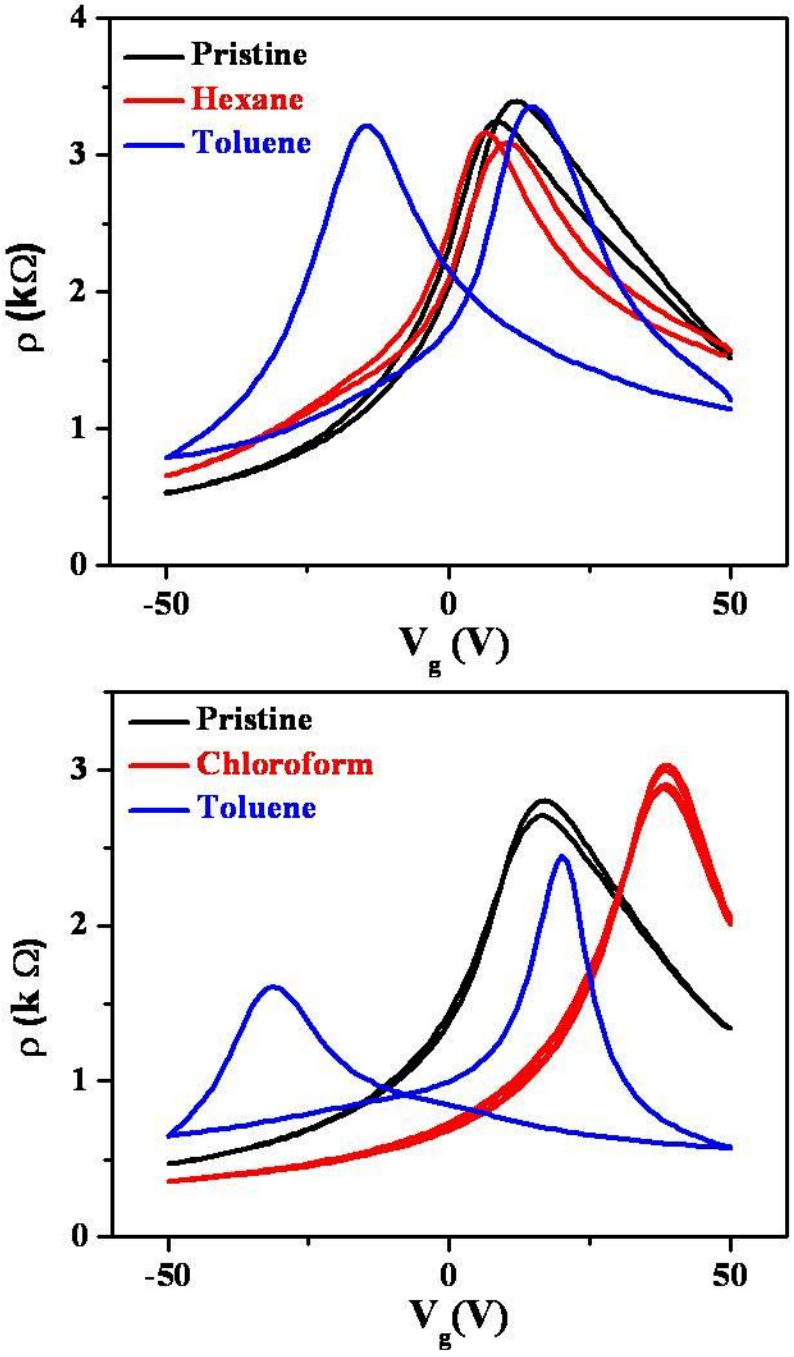

Figure IV-6 Resistivity vs gate voltage for samples before and after adding hexane and chloroform. There is no memory effect using these two solvents. Toluene molecules are also added to these samples. After toluene, large memory effect appears.

toluene molecules on the sample, the memory effect became stronger and stronger (Figure IV-7 (a)), indicated by more and more split between the two resistivity peaks. The same thing happened in the sample using naphthalene molecules. But the memory effect was not as strong as the sample using toluene (Figure IV-7 (b)). For the sample using anthrancene, no matter how much molecules were added, we do not observe a large memory effect (Figure IV-7 (c)). In this sample, after removing the anthrancene, we try toluene again and we find a large memory effect. This excludes the factor of sample variation. Graphene is known to have a positive 4.5 eV electron affinity [Sque, *et al.*, 2007, Buonocore, *et al.*, 2008], which is opposite to that of toluene. So the binding between graphene and toluene molecules can be good and the energy barrier at the interface is low, and the charge can be transferred between them easily. Finally, compared to other molecules, toluene molecules have similar hexagonal ring structure as graphene. They can easily form the nice stack configuration on top of graphene, which will also provide very good binding to the graphene surface.

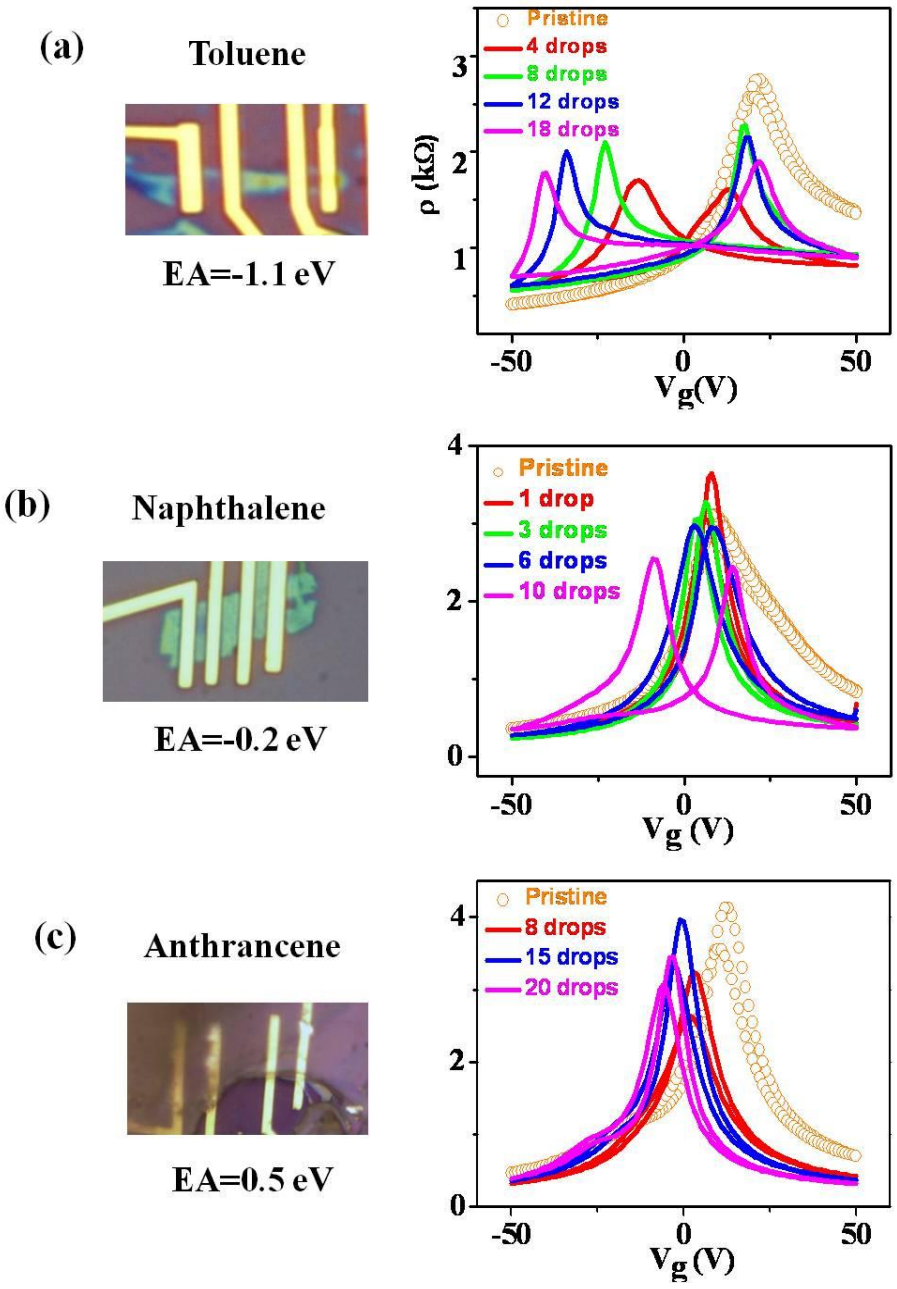

Figure IV-7 Left hand side: Optical images of devices dresses with toluene (a), naphthalene (b), and anthrancene (c) molecules. Righ hand side: For toluene or naphthalene, after adding more and more molecules, the memory effect becomes stronger and stronger. For anthrancene, no large memory effect is found no matter how much molecules are added.

IV-5 Conclusion

To conclude, in this chapter, we have discussed more details about the large memory effect in graphene device with a toluene molecules layer on top. We propose a possibility for making a graphene based memory device, in which no band gap is needed, and the mobility of graphene is not destroyed but increased. In addition, the reading and writing processes of this memory device are also discussed, as well as the possible reasons for this memory effect, which opens up a direction for more investigation.

Reference:

Zhang, Y. B., *et al.*, Nature 2007, 459, 820-823.

Han, M. Y., *et al.*, Phys. Rev. Lett. 2007, 98, 206805.

Wang, F., *et al.*, Science 2008, 320, 206-209.

Wang, H. M., *et al.*, ACS Nano 2010, 4, NO. 12, 7221–7228.

Liao, Z. M., *et al.*, J. Chem. Phys. 2010, 133, 044703.

Sque, S. J., *et al.*, Phys. Stat. Sol. 2007, 204, No. 9, 3078–3084.

Buonocore, F., *et al.*, Nanotechnology 2008, 19, 025711.

Chapter V
Thermoelectric Power in Graphene

V-1 Introduction

In addition to the electrical conductivity, thermoelectric power or TEP, which is the derivative of the energy-dependent electrical conductivity under certain conditions according to the Mott relation [Ashcroft, et al., 1976], provides a sensitive probe to study the transport properties of graphene as the Fermi energy can be conveniently tuned by a gate voltage [Lofwander *et al*., 2007, Zuev, *et al*., 2009, Wei, *et al*., 2009, Checkelsky, *et al*., 2009, Hwang, *et al.*, 2009]. From the temperature dependence of TEP, one can in principle distinguish different scattering mechanisms [Lofwander, *et al.* 2007]. The Mott relation is often applied to analyze TEP data in degenerate electron systems. In our work, we have prepared graphene devices with a wide range of carrier mobility, and therefore with a varying degree of disorders. As a starting point, we analyze our TEP data based on the Mott relation. First we found that in the area far way from graphene Dirac Point, the Seebeck coefficient diverges with $1/\sqrt{|n_{2D}|}$, where n_{2D} is the carrier density. This directly proves the linear dispersion of massless Dirac particles in graphene. Secondly, we also found that near Dirac Point there is a close relationship between the residual

carrier density due to charged impurities and the validity of the Mott relation. The results reported in this works are based measurements on 13 samples, with the carrier mobility μ_c ranging from 1,500 to 13,000 cm^2/Vs. Most graphene samples have both four electrodes plus a heater, but some have only two electrodes plus a heater, and some have only four electrodes for electrical measurements.

V-2 Thermoelectric Transport of Dirac Particles in Graphene

All the thermoelectric devices are fabricated in the method described in Chapter II. Figure V-1 is a false colored scanning electron micrograph of a device for both electrical conductivity σ and TEP measurements. For TEP, a temperature gradient, ∇T, is generated by a micro-fabricated heater, resulting in a thermal voltage response, V_{th}. Then Seebeck coefficient can be obtained by $S = \frac{V_{th}}{\Delta T}$. Electrodes 4 & 1 are the current leads, and electrodes 2 & 3 are the voltage leads for measuring both σ and V_{th}. This four-point (4P) geometry allows us to exclude the contact resistance and to ensure both σ and V_{th} to come from the same locations, where the local temperatures are measured by electrodes 2 & 3 via their 4P resistivity.

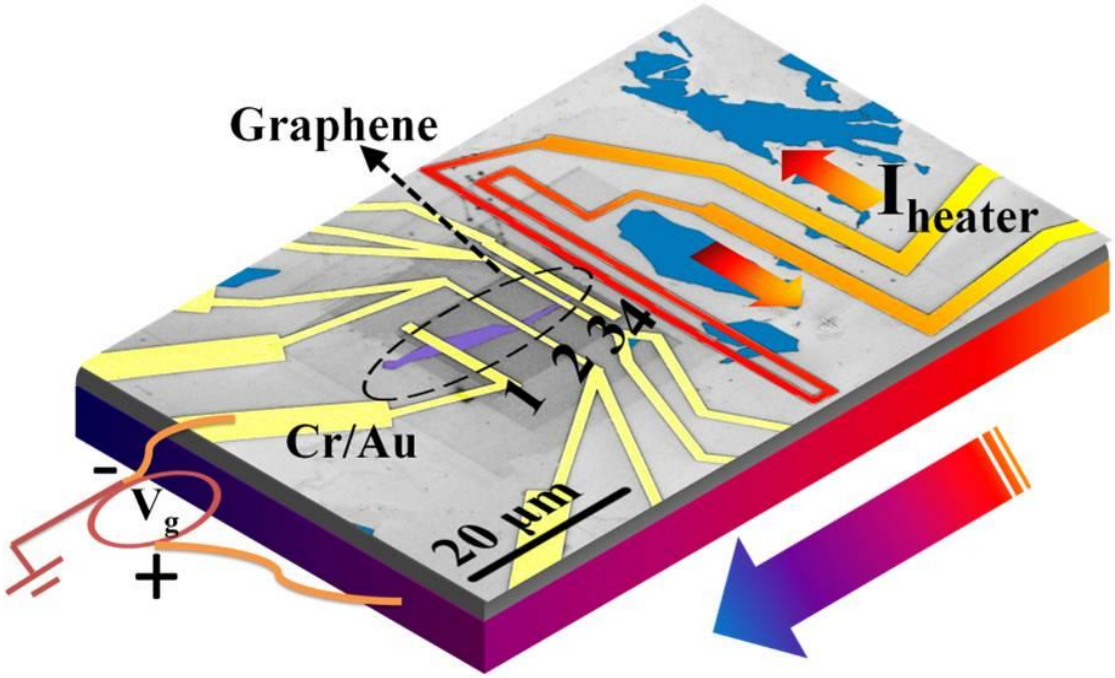

Figure V-1 A false colored scanning electron microscopy image of a graphene thermoelectric device. Electrode 2 & 3 are used for both conductivity and thermo voltage measurement.

The well known Mott relation is stated as the following:

$$S_C^{Mott} = -\frac{\pi^2 k_B{}^2 T}{3|e|}\frac{\partial \ln \sigma}{\partial \mu} \qquad (1)$$

where k_B, μ, and e are the Boltzmann constant, the chemical potential, and the electron charge, respectively. Generally, we can assume

$$\sigma \sim \mu^{\alpha} \qquad (2)$$

,where α is 1 for clean limit or 2 for dirty limit [Tan, *et al.*, 2007, Bolotin, *et al.* 2008]. Since grahpene is 2D system with linear energy dispersion, so for the chemical potential we have:

$$\mu = \hbar v_F \sqrt{n_{2D}\pi} \propto \pm\sqrt{|V_g - V_d|} \qquad (3)$$

where the + (-) sign corresponds to the electron (hole) doped regime, and v_F is the Fermi velocity. Combine equation (1), (2), and (3), we can finally get:

$$S \sim \frac{sgn(\mu)}{\sqrt{|V_g - V_d|}} \text{ or } \frac{1}{S^2} \sim |V_g - V_d| \qquad (4)$$

If 2D quadratic linear dispersion is used, where $\mu \propto n_{2D}$, Seebeck coefficient will be:

$$S \sim \frac{-1}{|V_g - V_d|} \text{ or } \frac{1}{S} \sim |V_g - V_d| \qquad (5)$$

Figure V-2 displays the $1/S^2$ vs V_g and $1/S$ vs V_g for a sample at three different temperatures. The mobility of this sample is 7000 $cm^2V^{-1}s^{-1}$. The dash straight lines are

(a)

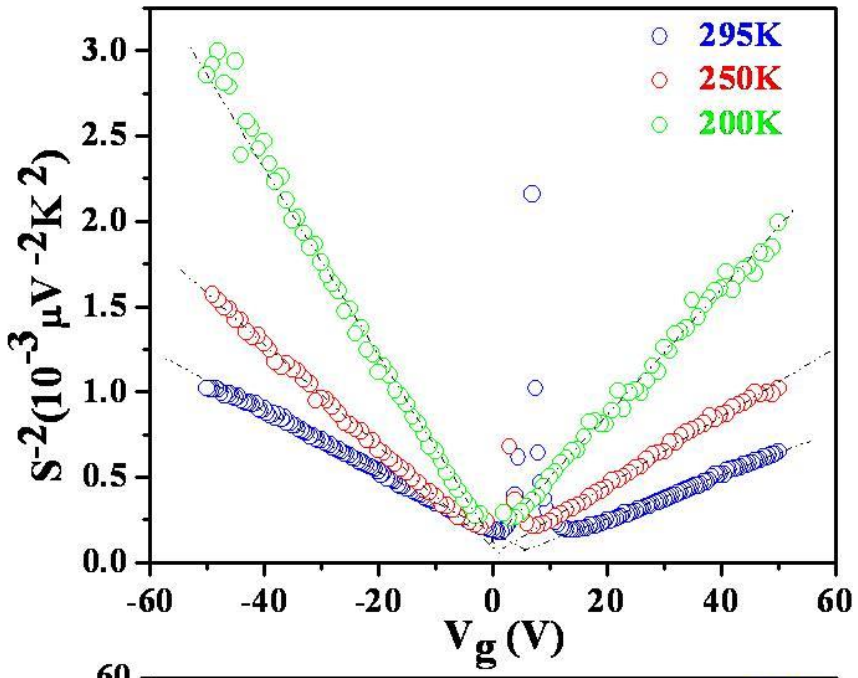

(b)

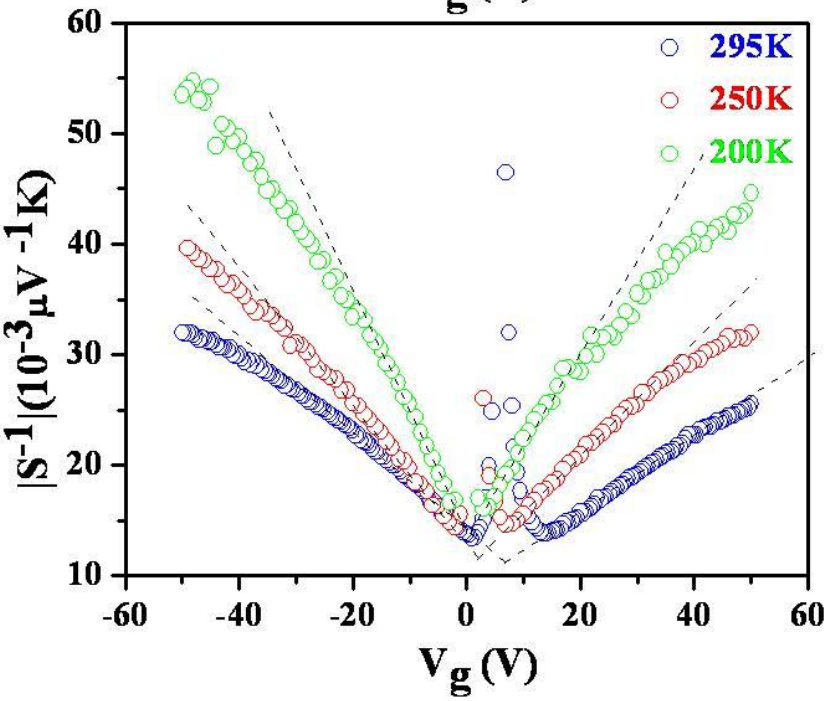

Figure V-2 $1/S^2$ vs V_g plot (a) and $1/|S|$ vs V_g plot (b) for a sample whose mobility is 7000 $cm^2V^{-1}s^{-1}$. The black dash lines are straight lines as guides to the eye.

drawn in the line region (far way from Dirac point). So clearly, $1/S^2$ vs V_g plot shows better linear relation with V_g over the whole gate range. Also $1/S^2$ extrapolates to zero at the Dirac point gate voltage but 1/S does not (the Dirac point voltage shifts when the device is cooled down from 295 K to 250 K). So this diverging behavior of S proves that the dispersion relation in graphene is linear rather than quadratic, as expected for Dirac particles. What should also be mentioned is the exponent α in equation (2) does not affect the functional dependence of S since it is absorbed in the prefactor of S.

V-3 Thermoelectric Power in Low and High Mobility Graphene Samples

Since we can four points geometry in the graphene devices, in which we can exclude the contact resistance, we can actually calculate S using the conductivity without any power law assumption of the σ. So if we rewrite the Mott relation in this way:

$$S_C^{Mott} = -\frac{\pi^2 k_B^2 T}{3|e|}\frac{\partial \ln\sigma}{\partial\mu} = -\frac{\pi^2 k_B^2 T}{3|e|}\frac{\partial \ln\sigma}{\partial V_g}\frac{\partial V_g}{\partial\mu} = -\frac{\pi^2 k_B^2 T}{e3|}\frac{\partial \ln\sigma}{\partial V_g}\left(\frac{e}{c}\frac{\partial n_{2D}}{\partial\mu}\right)^{-1} \qquad (6)$$

We use $\frac{\partial V_g}{\partial\mu} = \frac{e}{c}\frac{\partial n_{2D}}{\partial\mu}$, where the capacitance per unit area C is 115 $aF/\mu m^2$ for our device geometry, and $\frac{\partial n_{2D}}{\partial\mu}$, the single-particle density-of-states, is determined from the dispersion relation. From equation (6), we can get a calculated S_C^{Mott}. Figure V-3 shows a measured S_M (open circles) and three calculated S_C^{Mott} (solid lines) from a sample with

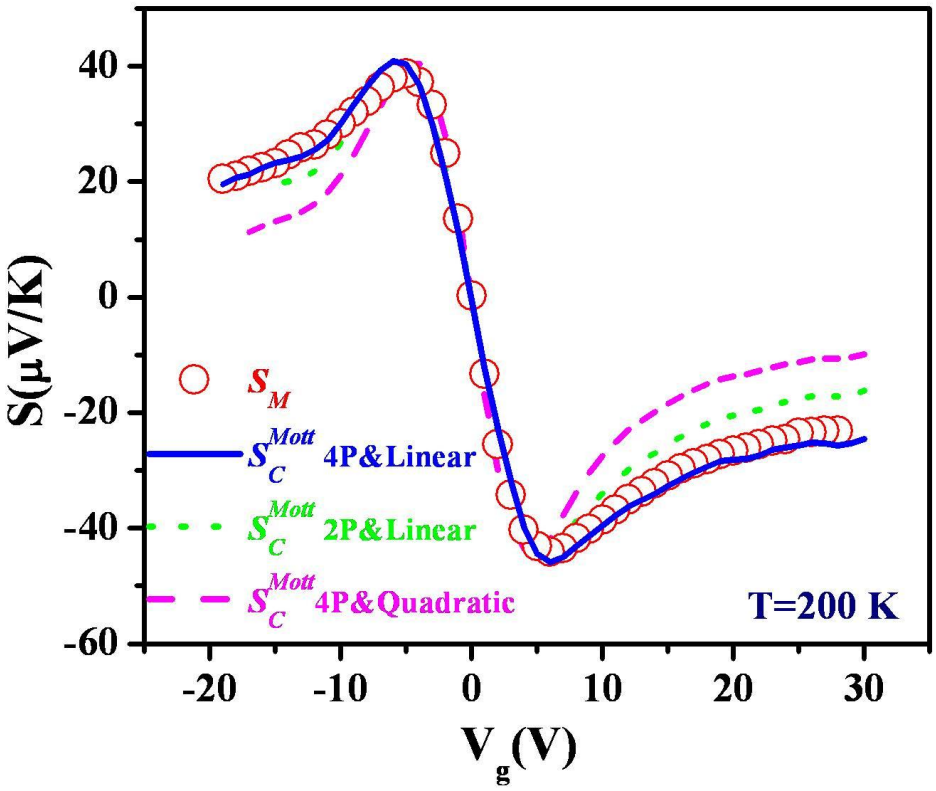

Figure V-3 Comparison of experimentally measured Seebeck coefficient S_M (open circles) and three Seebeck curves S_C^{Mott} calculated from measured electrical conductivity using the Mott relation. The blue curve is calculated with the 4P resistivity and a linear dispersion relation; green dots are with the two-point (2P) resistivity and a linear dispersion relation; and magenta dash line is with the 4P resistivity and a quadratic dispersion relation. μ_c of this device is ~ 1,500 cm^2/Vs.

mobility 1500 $cm^2V^{-1}s^{-1}$. First of all, a quadratic dispersion produces the largest discrepancy with S_M(magenta), even using the 4P resistivity which does not include the contact resistance (~ 4,500 Ω), indicating that the single-layer graphene does not follow the quadratic dispersion relation for particles with a mass. Using a linear dispersion relation, we calculate S_C^{Mott} from σ measured with both the two-point (green) and 4P (blue) methods and yield better agreement with S_M. The best agreement is reached with the 4P resistivity, which suggests that the Mott relation holds for all V_g if the graphene resistivity is properly measured by the 4P method and a linear dispersion relation is used.

We find that the local resistive thermometry reports a larger∇T, which is likely caused by the high thermal conductivity of graphene [Seol, *et al.*, 2010, Ghosh, *et al.* 2010]. This occurs because the local thermometers, i.e. segments of Au/Cr electrodes, are actually much longer than the width of the graphene device (Figure V-1); therefore, the temperature rise of the thermometers is primarily determined by the substrate, which consequently overestimates ∇T on graphene and underestimates the magnitude of S_M. We have verified this by comparing the resistance change of the thermometers with that of the graphene probed between electrodes 1&2, 2&3, and 3&4. The discrepancy in the resulting ∇T evaluated from these two methods can be as large as a factor of two. However, for a fixed temperature, ∇T should remain constant as V_g is swept;

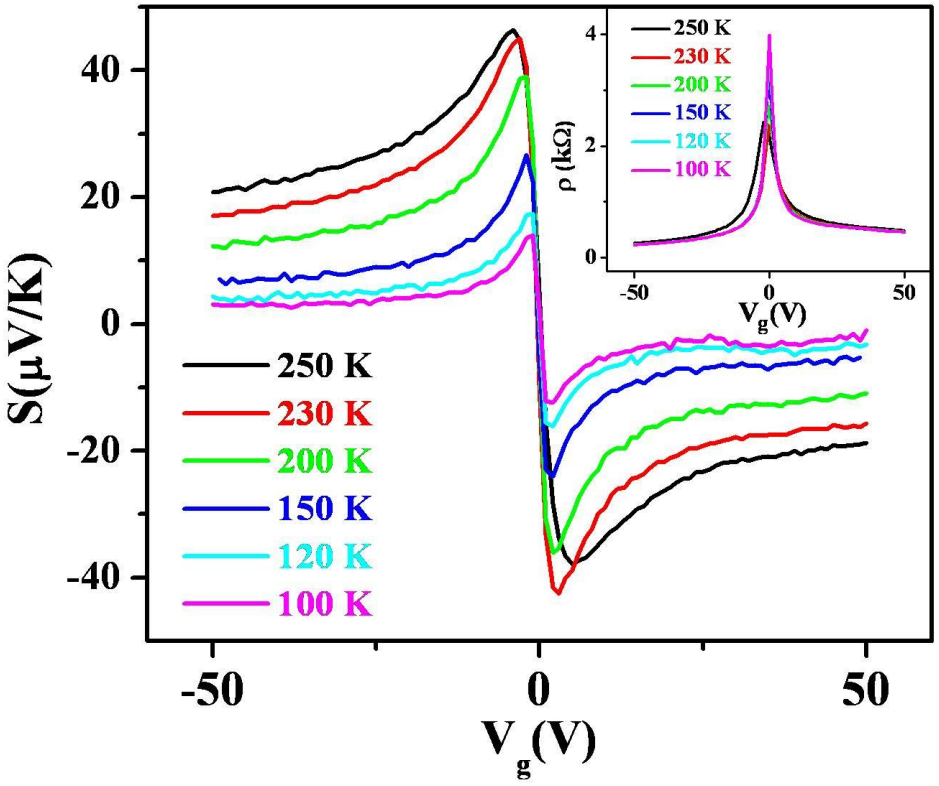

Figure V-4 Seebeck coefficients of a device (μ~ 13000 $cm^2V^{-1}s^{-1}$) measured from T = 100 to 250 K. The 4P resistivity data are shown in the inset.

therefore, the measured and calculated TEP should only differ by a V_g-independent factor. In Figure V-2 we allow an adjustable parameter to match the calculated TEP curves with S_M. The blue curve clearly matches the data best. If the Fermi velocity of 1×10^6 m/s is used, the V_g-independent calibrator factor is found to be about two.

Although similar satisfactory agreement is found in other low-μ_c samples, high-μ_c samples exhibit a quite different behavior. Figure V-4 is the TEP data on a much higher μ_c sample (~ 13,000 cm^2/Vs). S_M shows a more diverging trend and a sharp peak and dip near the Dirac point or the charge neutral point (CNP) at all temperatures. Moreover, the diverging Seebeck can be very well fitted by $\sim \frac{1}{\sqrt{|V_g - V_D|}}$ on both sides except over the central region defined bounded by the peak and dip. ΔV, the peak-to-dip width in V_g, is about 5 V at 200 K, narrower than that in the low-μ_c sample, i.e. ~10 V in Figure V-3. Figure V-5 shows the similar Mott relation analysis using a linear dispersion and 4P resistivity for four selected temperatures. At 100 K, S_M and S_C^{Mott} agree well over the whole V_g range. At higher temperatures, a deviation starts to develop near CNP and grows progressively both in the magnitude and the V_g range. The same qualitative behaviors are observed in other high-μ_c samples. Due to the aforementioned uncertainty in local temperature measurements, we also allow a V_g-independent factor to match the calculated data with S_M at each temperature. We expect the Mott relation to hold at high

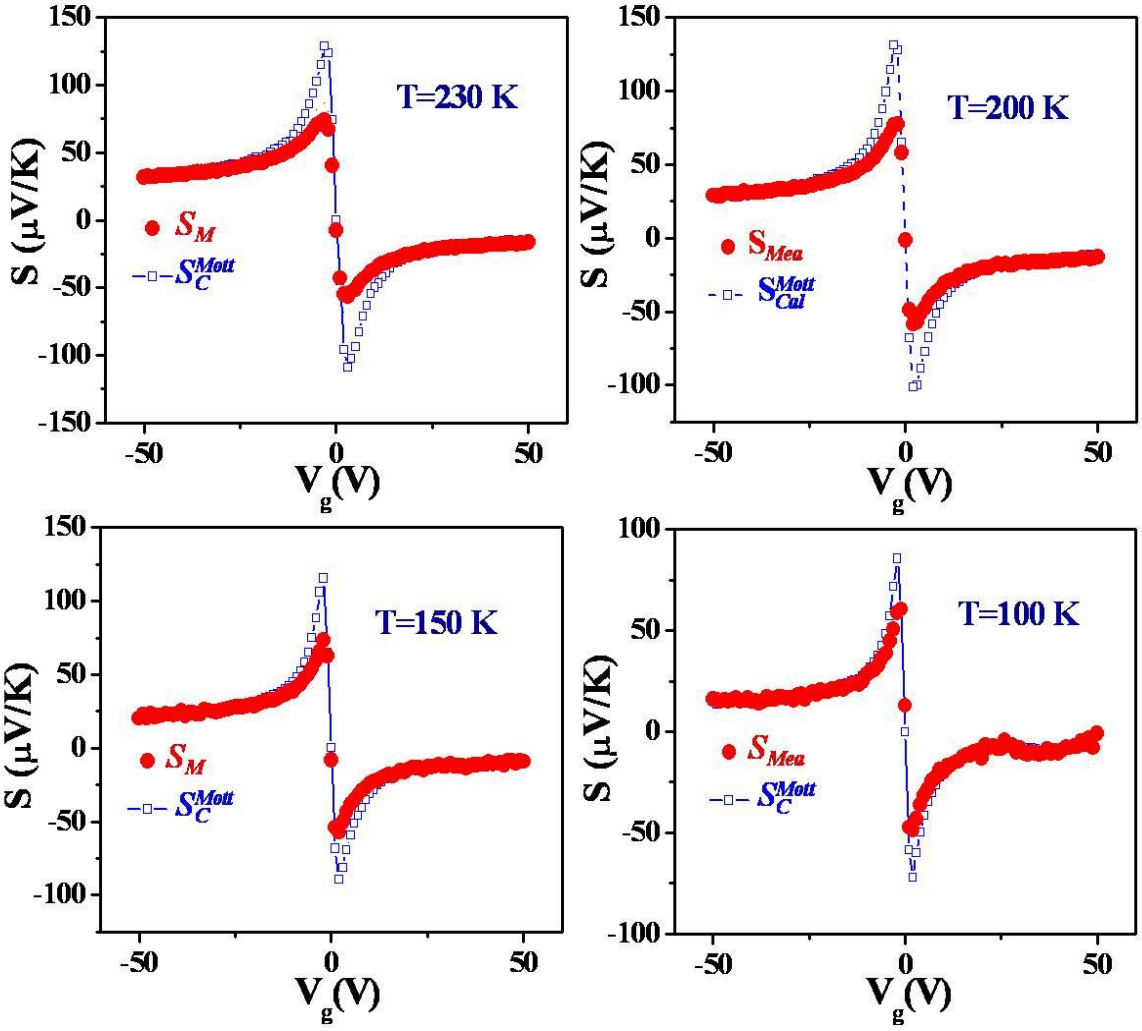

Figure V-5 Comparison of experimentally measured S_M (open circles) and calculated S_C^{Mott} (solid blue curves) at four temperatures. The 4P resistivity, a linear dispersion and Mott relation are used.

V_g where the carriers are degenerate; therefore, we force S_C^{Mott} with S_M to match at the highest V_g. Note that the peak/dip features in S_C^{Mott} are quite sharp. It is impossible to match these features by varying the adjustable parameter.

The connection between the magnitude of μ_c and the deviations from the Mott relation calculation is better seen in Figure V-6. A comparison is made between S_M and S_C^{Mott} in four samples with different μ_c. All measurements were performed at the same temperature, T=200 K. Evidently, the Mott relation holds for the lowest μ_c sample, but deviates most significantly in the highest μ_c. At low temperatures (below 100 K), the deviation is insignificant even in the highest μ_c samples (data not shown). More interestingly, this trend is observed in a device whose μ_c can be set at different values (Figure V-7). In Chapter III, we showed that μ_c can be widely tuned using molecules which modify graphene's charge environment. In this device, μ_c at 295 K can be tuned by a factor of two. The contrast between these two cases confirms that the validity of the Mott relation is intimately related to μ_c.

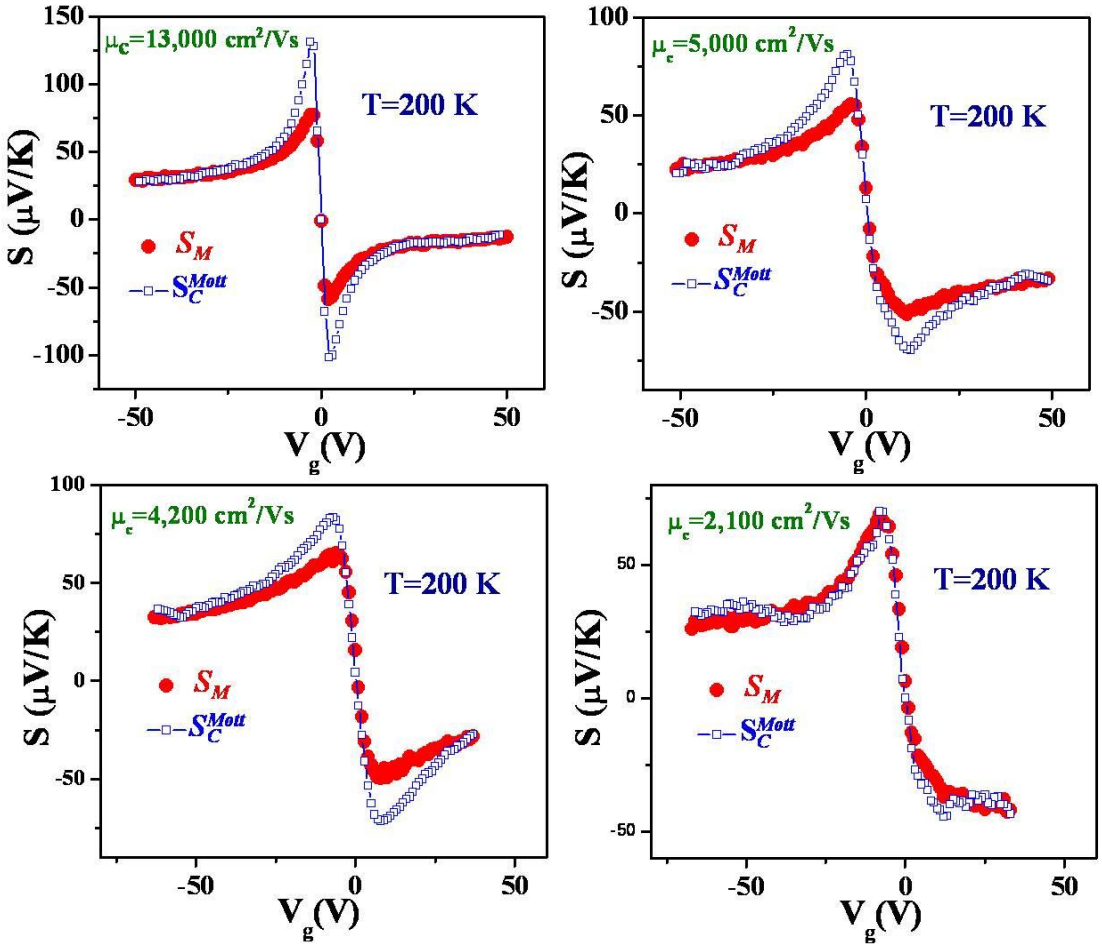

Figure V-6 Comparison of experimentally measured (S_M, red solid dots) and calculated (S_C^{Mott}, blue open square and line) Seebeck coefficient for four graphene samples with different μ_c values (from 2,100 to 13,000 $cm^2V^{-1}s^{-1}$) at T = 200 K.

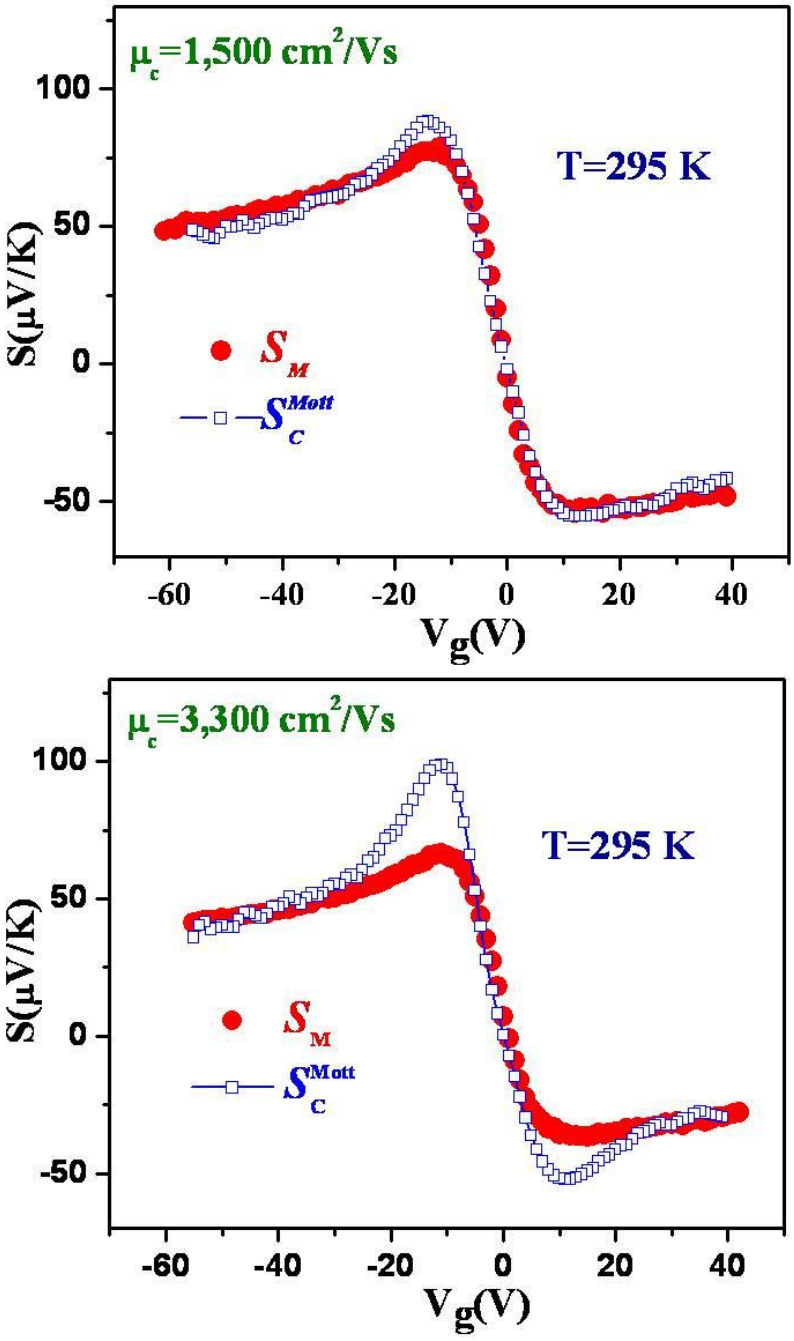

Figure V-7 Comparison of the data from one device with two different μ_c values (1,500 and 3,300 $cm^2V^{-1}s^{-1}$)

V-4 Charge Impurity Model and Fermi Temperature

The Mott relation is obtained from the Boltzmann equation which is applicable for single-electron systems. Failure of the Mott relation could indicate that the electron-electron interaction in high-μ_c samples becomes important near CNP. However, the fact that it fails only at higher temperatures argues strongly against such a scenario. On the other hand, the Mott relation is an approximation for degenerate electron systems when T is far below the Fermi temperature T_F. In the language of the linear response theory,

$$S = \frac{L^{12}}{L^{11}}, \text{ where } L^{11} = \ell^{(0)}, L^{12} = -\frac{1}{Te}\ell^{(1)}$$

and

$$\ell^{(\alpha)} = \int d\varepsilon(-\frac{\partial f}{\partial \varepsilon})(\varepsilon-\mu)^{(\alpha)}\sigma(\varepsilon) \qquad (7)$$

$f(\varepsilon) = \frac{1}{e^{(\varepsilon-\mu)k_BT}+1}$ is the Fermi-Dirac distribution function. L^{11} and L^{12} are two coefficients in the linear transport equations and L^{11} is simply the electrical conductivity. Under the condition $k_BT << \mu$, $\left(-\frac{\partial f}{\partial \varepsilon}\right)$ can be legitimately replaced by the delta-function and the leading order in S yields the Mott relation. However, the carrier density near CNP can be so low that $k_BT << \mu$ no longer holds; consequently, the Mott relation is violated. This is what precisely occurs in high-μ_c graphene because the low-density region near

CNP renders $k_BT << \mu$ invalid. In low-μ_c graphene, on the other hand, the charged impurities are bountiful, so are the electron and hole puddles in the vicinity of CNP. In the charged impurity model [Adam, *et al.*, 2007, Chen, *et al.*, 2008], the impurity density n_{imp} determines μ_c by

$$\mu_c = (\frac{20e}{h})\frac{1}{n_{imp}} \qquad (8)$$

Although the net charge density can be small near CNP, the residual local charge fluctuation, n^*, can be significantly large, which implies the absence of the low-density region near CNP.

According to the theory, n^* can be determined from both μ_c and the minimum conductivity $\sigma_{\min}$ as the following:

$$\sigma_{\min} = n^* e \mu_c \qquad (9)$$

We calculate relevant parameters from μ_c and $\sigma_{\min}$ for all devices. As shown in Table V-1 (five samples with different mobility), both n_{imp} and n^* can vary by an order of magnitude from sample to sample. The same thing is found in Table V-2 where the data is obtained from one sample whose mobility is tuned. As a result, the calculated T_F can be as low as 359 K in the highest-μ_c sample but as high as 1,458 K in the lowest-μ_c sample. The complete T_F vs. μ_c data are shown in the inset of Figure V-8. Below, we try to assess this effect in terms of a calculated V_g range based on the charged impurity model. We

convert n^* to an effective gate voltage ΔV_{Cal}^{Imp} using

$$\Delta V_{Cal}^{Imp} = \frac{|e|}{C} n^* \qquad (10),$$

which is the equivalent gate voltage that produces the corresponding carrier density n^* electrostatically. Then the region from - $n^*/2$ to $n^*/2$ in residual density defines a region near CNP where the transport is governed by electron and hole puddles, the same source for the $\sigma_{\min}$ plateau [Tan, *et al.*, 2007]. The calculated width of this region is plotted in Figure V-8 (blue and green). The blue symbols represent the data from 9 different devices with various μ_c values. The green symbols are the data taken from one device whose Seebeck coefficient data were shown in Figure V-4, and the variable μ_c in this device is obtained by manipulating the charge environment in graphene using molecules which is described in detail in Chapter III. These two sets of n^* data are calculated from the electrical conductivity data of different devices taken under different conditions. Surprisingly, the calculated ΔV from those two sets of data overlap well with each other when they meet in the intermediate μ_c range. For comparison, the red symbols are the width of the central region measured from the peak to dip in TEP. Apparently, the width defined by the peak-to-dip from the Seebeck curves is slightly larger than that determined from n^*, which can be attributed to the somewhat arbitrary criterion we adopted in defining the region. One is essentially defined by the region of the minimum conductivity plateau, while the other is by reading off the V_g values at the peak and dip in S_M.

μ_c (cm^2/Vs)	σ_{min} (e^2/h)	n_{imp} (cm^{-2})	n^* (cm^{-2})	T_F (K)
13,000	9.5	$3.8*10^{11}$	$1.8*10^{11}$	578
5,100	8.3	$1*10^{12}$	$2.9*10^{11}$	731
4,200	7.2	$1.2*10^{12}$	$4.3*10^{11}$	885
2,100	6.9	$2.3*10^{12}$	$7.8*10^{11}$	1,200
1,500	7.0	$3.3*10^{12}$	$1.2*10^{12}$	1,458

Table V-1 Carrier mobility μ_c, minimum conductivity σ_{min}, charged impurity density n_{imp}, residual carrier density n^*, and the Fermi temperature T_F for five representative graphene devices.

μ_c (cm^2/VS)	σ_{min} (e^2/h)	n_{imp} (cm^{-2})	n^* (cm^{-2})	T_f (K)
19000	5.4	$2.6*10^{11}$	$7.0*10^{10}$	359
16000	5.6	$3.1*10^{11}$	$8.7*10^{10}$	400
15300	7.7	$3.3*10^{11}$	$1.3*10^{11}$	479
13100	8.3	$3.8*10^{11}$	$1.6*10^{11}$	540
9500	9.4	$5.3*10^{11}$	$2.5*10^{11}$	675
7700	11.3	$6.5*10^{11}$	$3.7*10^{11}$	823
4600	14.0	$1.1*10^{12}$	$7.6*10^{11}$	1180

Table V-2 Carrier mobility μ_c, minimum conductivity σ_{min}, charged impurity density n_{imp}, residual carrier density n^*, and the Fermi temperature T_F for one graphene device whose mobility can be tuned.

Both decrease as μ_c increases in the same trend, which indicates that the physics near CNP is governed by the residual local charge density.

If n^* is so large that $T_F \gg T$, the low-temperature approximation is valid, and then we would expect the Mott relation to hold. This is indeed the case in low-μ_c devices. If the opposite is true, the Mott relation is violated, which is the case in high-μ_c samples. As V_g is swept from high positive values, the net charge density is high and so is T_F. As it approaches CNP, both the net and residual charge densities are low in high-μ_c samples; therefore, the low carrier density or low T_F region is reached, consequently, the Mott relation fails. It becomes operative again when the hole density is sufficiently high as V_g is swept to more negative values

V-5 Boltzmann Transport Theory Approach

In the low density central region where the Mott relation fails, it is still possible to calculate the Seebeck coefficient from Equation (7). At finite temperatures, three factors must be considered: full $(-\frac{\partial f}{\partial \varepsilon})$ function, T-dependent chemical potential $\mu(T)$, and the energy dependent kernel function, $\sigma(\varepsilon)$. We adopt an earlier result for $\mu(T)$, as shown by Eq. 17 in [Hwang, *et al.,* 2009]. $\sigma(\varepsilon)$ can explicitly depend on T via electron-phonon

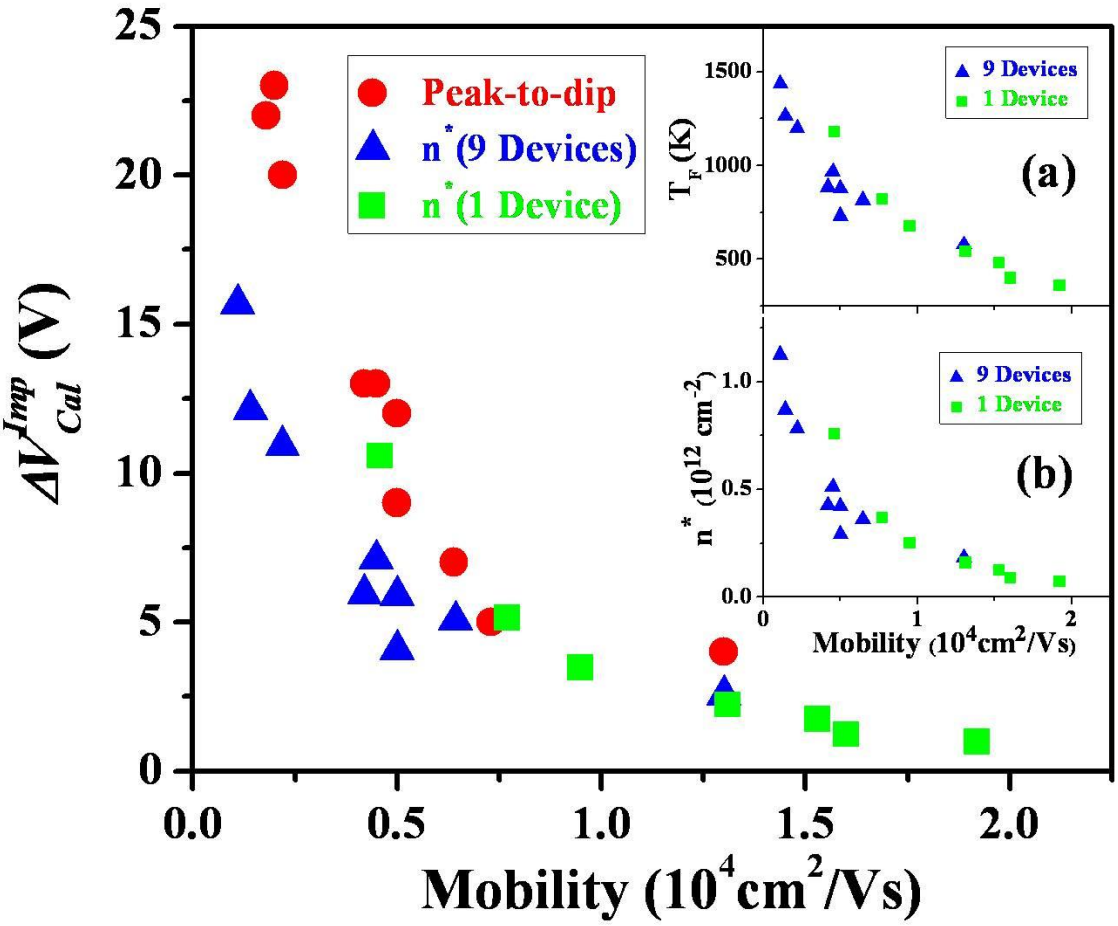

Figure V-8 Gate voltage range corresponding to the residual charge density range from –n*/2 to n*/2 in devices with varying μ_c values. Blue triangles are calculated from the data taken at T= 200 K in 9 different devices, whereas green squares are from one device but with a range of μ_c values at 20 K. Red circles represent the peak-to-dip gate voltage range in measured Seebeck coefficient. Insets (a) and (b) show the calculated Fermi temperature T_F and residual carrier density n^* vs. μ_c for all devices, respectively.

interaction and/or dielectric constant due to screening. Although these effects on the kernel function have been addressed theoretically [Hwang, *et al.*, 2009], here we attempt to assess the temperature effects using V_g-dependednt conductivity, i.e. L[11], which is actually measured in our experiments.

We use Mathematica to calculate the Seebeck coefficient by using measured conductivity. From equation (7), we can get

$$S = [-\frac{1}{\mathrm{Te}}\int d\varepsilon(-\frac{\partial f}{\partial \varepsilon})(\varepsilon-\mu)\ \sigma(\varepsilon)]/\sigma_T \qquad (11)$$

where σ_T is the measured conductivity. For the energy dependent kernel function $\sigma(\varepsilon)$. We do the approximation by (a) replacing $\sigma(\varepsilon)$ by measured low-T conductivity, denoted as $S_{Cal}^{Full}(a)$; (b) replacing $\sigma(\varepsilon)$ by measured finite-T conductivity, denoted as $S_{Cal}^{Full}(b)$. To calculate the integral on the top, we first need to get a function for the $\sigma(\varepsilon)$. In Mathematica, we use the polynomial to fit the data. Figure V-9 displays the low-T conductivity data (dots) and the polynomial fitting (solid line). We can see that the fitting works very well on the data. $(-\frac{\partial f}{\partial \varepsilon})$ is a delta function in the condition when $\mu >> k_B T$. When in the opposite case, $(-\frac{\partial f}{\partial \varepsilon})$ is not a delta function and it is already zero as $|\varepsilon| > 5\mu$. So for the integral interval in equation (11), we use [-5μ, 5μ] instead of $[-\infty, +\infty]$.

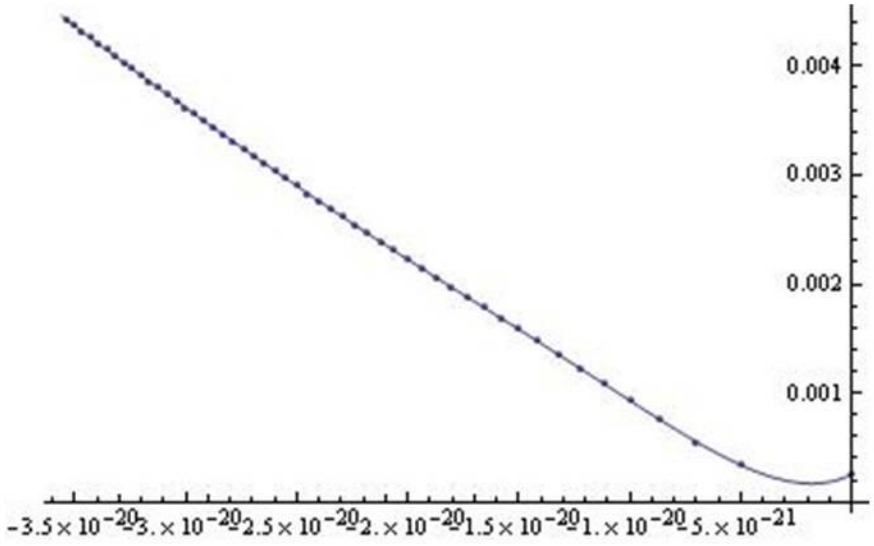

ε<0

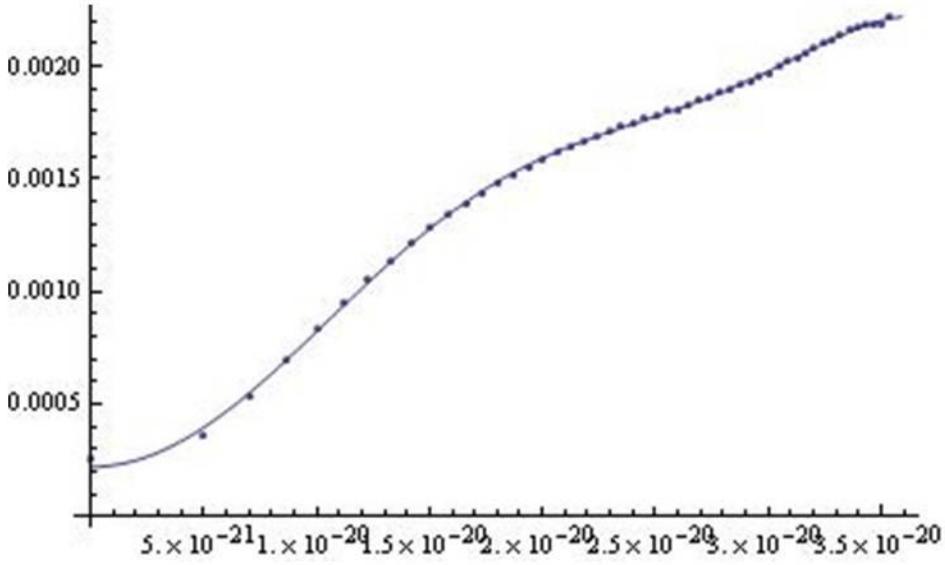

ε>0

Figure V-9 The σ vs ε data (dots) and the polynomial fitting (solid line) using Mathematica

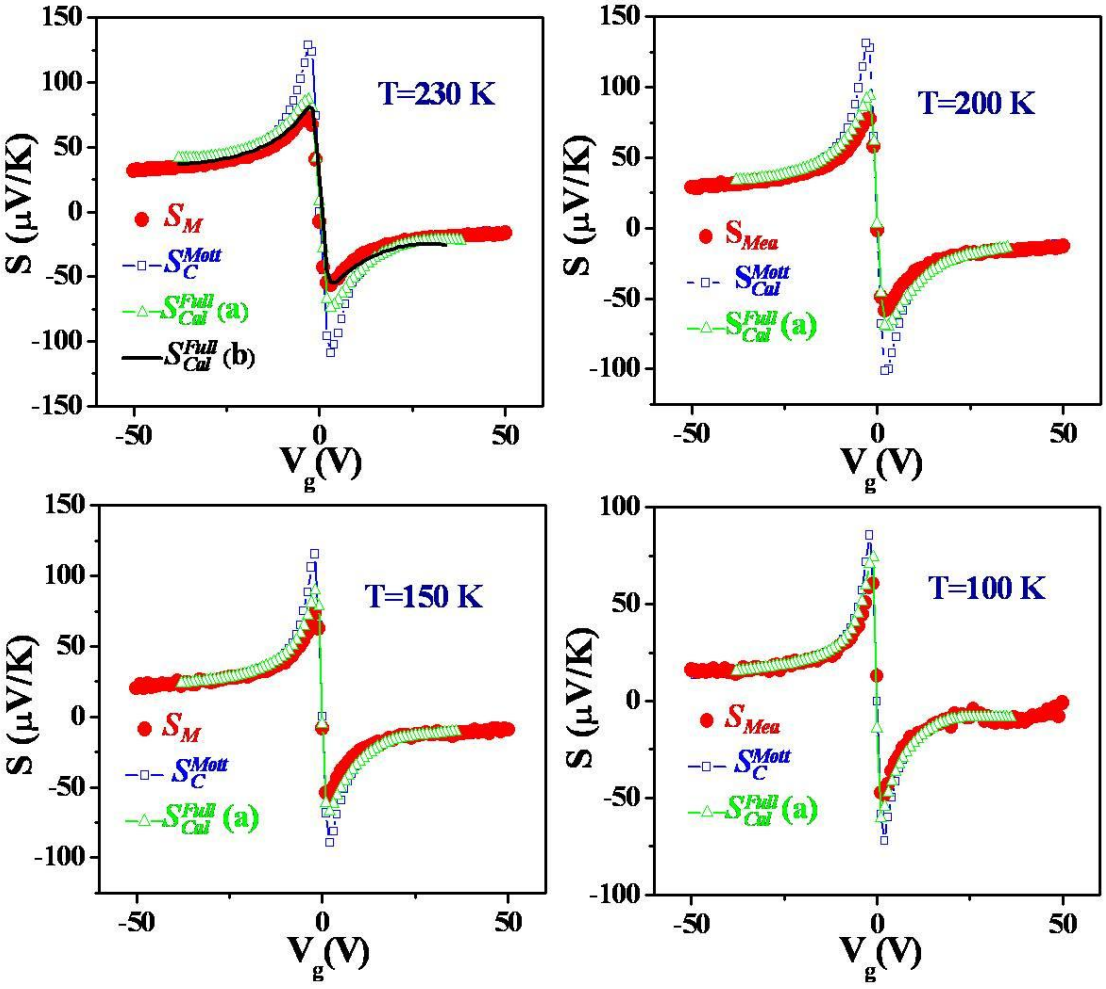

Figure V-10 Comparison of experimentally measured S_M (open circles) and calculated (solid curves) Seebeck coefficient at four temperatures. The 4P resistivity and a linear dispersion relation are used for all cases. Blue curves (S_C^{Mott}) are the results calculated from the Mott relation. Green curves ($S_{Cal}^{Full}(a)$)are calculated using Eq. 11 with σ(ε) measured at T = 100 K. The black curve ($S_{Cal}^{Full}(b)$)for T= 230 K is also calculated using Eq. 11 but with σ(ε) measured at T= 230 K.

Using the fitting function of $\sigma(\varepsilon)$ (low-T and finite-T), by numerical integral on equation (11), we can get $S_{Cal}^{Full}(a)$ and $S_{Cal}^{Full}(b)$, which are shown as the green and black curves in the upper left panel of FigureV-10. Obviously, $S_{Cal}^{Full}(a)$ leaves out the explicit *T*-dependence of $\sigma(\varepsilon)$, which inevitably underestimates the effects of temperature in L^{12}. $S_{Cal}^{Full}(b)$ uses the measured finite-*T* conductivity which already includes the effect of the energy spread in $f(\varepsilon)$ along with other temperature effects such as the screening and phonons. In principle, this latter approximation overestimates the temperature effect. Clearly, both approximations yield better agreement with the experimental data than the Mott relation calculations. The second approximation appears to be slightly better, which indicates that the effects of screening and phonons on σ are important at high temperatures. The other panels in Figure V-10 only contain $S_{Cal}^{Full}(a)$ curves.

V-6 Conclusion

We have studied TEP along with the electrical transport and examined the Mott relation in over a dozen graphene samples with a wide range of μ_c values. In high-μ_c samples that have low residual carrier densities n^*, the Mott relation is violated in the vicinity of CNP, which is in contrast to poor μ_c samples in which the Mott relation is found to always hold over the entire gate voltage range. Finally, the Boltzmann transport

taking a proper account of the temperature effects can satisfactorily explain the experimentally measured Seebeck coefficient near CNP.

Reference:

Ashcroft, N. W. and Mermin, N. D., 1976, *Solid State Physics*.

Zuev, Y. M., *et al.*, Phys. Rev. Lett. 2009, 102, 096807.

Wei, P. *et al.*, Phys. Rev. Lett. 2009, 102, 166808.

Checkelsky, J. G., *et al.*, Phys. Rev. B 2009, 80, 081413.

Lofwander, T., *et al.*, Phys. Rev. B 2007, 76, 193401.

Hwang, E. H., *et al.*, Phys. Rev. B 2009, 80, 235415.

Seol, J. H., *et al.*, Science 2010, 328, 213.

Ghosh, S., *et al.*, Nature Mater. 2010, 9, 555.

Adam, S., *et al.*, Proc. Nat. Acad. Sci. 2007, 104, 18392.

Chen J. H., *et al.*, Nature Phys. 2008, 4, 377.

Tan, Y. W., *et al.*, Phys. Rev. Lett. 2007, 99, 246803

Hwang, E. H., *et al.*, Phys. Rev. B 2009, 79, 165404